



ELSEVIER

Nuclear Physics A 703 (2002) 3–44

www.elsevier.com/locate/npe

Wobbling phonon excitations, coexisting with normal deformed structures in ^{163}Lu

D.R. Jensen ^a, G.B. Hagemann ^{a,*}, I. Hamamoto ^b, S.W. Ødegård ^{c,a},
M. Bergström ^a, B. Herskind ^a, G. Sletten ^a, S. Törmänen ^a, J.N. Wilson ^a,
P.O. Tjøm ^c, K. Spohr ^d, H. Hübel ^e, A. Görge ^e, G. Schönwasser ^e,
A. Bracco ^f, S. Leoni ^f, A. Maj ^g, C.M. Petrache ^{h,i}, P. Bednarczyk ^{g,j},
D. Curien ^j

^a The Niels Bohr Institute, Blegdamsvej 17, DK-2100 Copenhagen Ø, Denmark

^b Department of Mathematical Physics, LTH, University of Lund, Lund, Sweden

^c Department of Physics, University of Oslo, PB 1048 Blindern, N-0316 Oslo, Norway

^d Department of Electronic Engineering and Physics, University of Paisley, Paisley, Scotland, UK

^e ISKP, University of Bonn, Nussallee 14-16, D-53115 Bonn, Germany

^f Dipartimento di Fisica and INFN, Sezione di Milano, Milano, Italy

^g Niewodniczanski Institute of Nuclear Physics, Krakow, Poland

^h Dipartimento di Fisica and INFN, Sezione di Padova, Padova, Italy

ⁱ Dipartimento di Matematica e Fisica, Università di Camerino, Camerino, Italy

^j IReS, 23 rue du Loess, BP28 F-67037, Strasbourg, France

Received 15 October 2001; accepted 15 November 2001

Abstract

Wobbling is a rotational mode unique to a triaxial body. The Lu–Hf isotopes with $N \sim 94$ at high spin provide a possible region of nuclei with pronounced triaxiality. We have investigated ^{163}Lu through the fusion-evaporation reaction $^{139}\text{La}(^{29}\text{Si}, 5n)^{163}\text{Lu}$ with a beam energy of 152 MeV. Three excited bands decaying into the known, presumably triaxial, superdeformed (TSD) band built on the $i_{13/2}$ proton orbital are observed. The electromagnetic properties of the connecting transitions from the two strongest populated excited TSD bands have been investigated. New particle-rotor calculations in which one $i_{13/2}$ quasiproton is coupled to the core of triaxial shape produce a variety of bands, whose properties can clearly be interpreted either as “wobbling” or “cranking” motion of the core. Evidence for the assignment of the excited TSD bands as one, and possibly even two wobbling phonon modes built on the yrast TSD band in ^{163}Lu is given. These triaxial bands coexist with bands built on quasiparticle excitations in the normal deformed (ND) minimum for which new data are also presented. © 2001 Elsevier Science B.V. All rights reserved.

PACS: 21.10.-k; 21.10.Re; 23.20.En; 27.70.+q

* Corresponding author.

E-mail address: hagemann@talws20.nbi.dk (G.B. Hagemann).

1. Introduction

A family of rotational bands with the characteristics of superdeformed (SD) structures have been observed in several Lu isotopes. In the even N isotopes $^{163-167}\text{Lu}$ [1–4] the bands are based on the strongly deformation driving proton $i_{13/2}$ configuration, while in odd-odd ^{164}Lu [5], the $i_{13/2}$ proton is coupled to different neutron orbitals. Similar bands have also been observed in the even-even nucleus, ^{168}Hf [6]. Lifetimes have been measured for the yrast SD bands in ^{163}Lu [2,7], ^{164}Lu [7] and ^{168}Hf [6] from which transition quadrupole moments are derived that are substantially larger than those of normal-deformed (ND) bands in this mass region. They range from $Q_t \sim 7.1$ b in ^{164}Lu to $Q_t \sim 11.4$ b in ^{168}Hf . In all these observed bands, the dynamic moments of inertia are similar and larger than for bands built on normal deformed (ND) structures in the same nuclei.

As a general property for nuclei in the $Z \sim 71$, $N \sim 94$ mass region, cranking calculations with the “Ultimate Cranker” code (UC) [8,9], based on a modified harmonic oscillator potential, predict local minima in the total energy surface for quadrupole deformations of $\epsilon_2 \sim 0.4$ with a triaxiality of $\gamma \sim \pm 20^\circ$. Fig. 1 shows as an example a surface calculated for ^{163}Lu for $I = 53/2\hbar$ and $\pi = +$, illustrating the ND minimum together with the local minimum at $\epsilon_2 \sim 0.4$, $\gamma \sim +20^\circ$. In general, the local minima with positive value of γ are found at lower energy than the minima with negative value of γ . The triaxial minima are found for all combinations of parity and signature, and

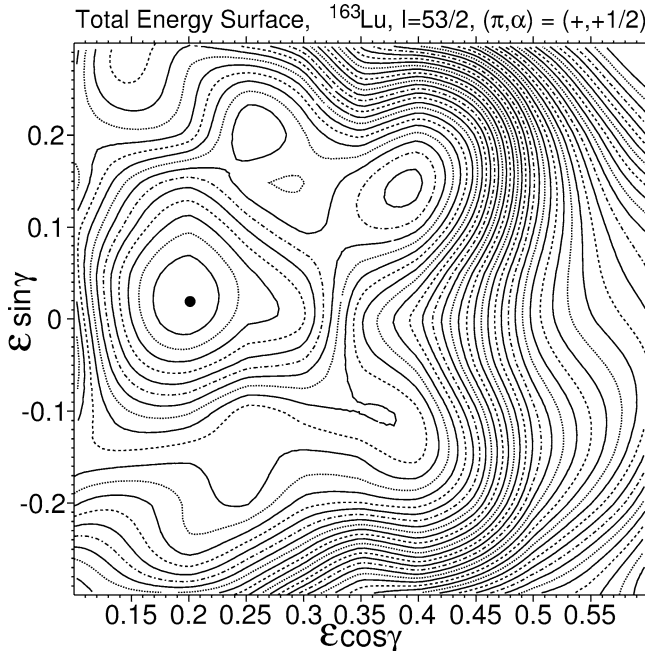


Fig. 1. Total energy surface for ^{163}Lu for $I^\pi = 53/2^+\hbar$. The ND minimum together with the local minimum at $(\epsilon_2 \sim 0.4, \gamma \sim +20^\circ)$ are clearly seen while the local minimum at $(\epsilon_2 \sim 0.4, \gamma \sim -20^\circ)$ is rather poorly developed at this spin value.

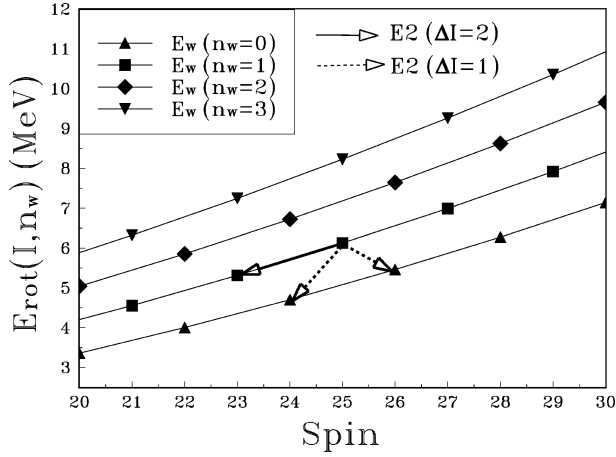


Fig. 2. Schematic wobbling pattern in the absence of aligned particles simulated with $\omega_{\text{wob}}/\omega_{\text{rot}} = 3$.

believed to have their origin from a pronounced shell gap at $N = 94$ in the triaxial neutron system.

No direct experimental evidence of the triaxiality of these bands has so far been found, and their interpretation as triaxial superdeformed (TSD) bands has been based on the calculated properties. However, one unique consequence of a rotating nucleus with a triaxial shape would be the existence of “wobbling bands”, an excitation mode predicted more than 25 years ago [10], but until now never observed in experiment. For a triaxial body with different moments of inertia with respect to the principal axes, $\mathcal{I}_x \gg \mathcal{I}_y \neq \mathcal{I}_z$, and in the high spin limit with most of the spin aligned along the x axis, the wobbling bands can be represented by a sequence of bands with increasing number of wobbling quanta, $n_w = 0, 1, 2, \dots$. This is illustrated in Fig. 2 where the characteristic pattern of the competition between the in-band transitions and the decay between the bands are indicated. The possible presence of the angular momentum coming from intrinsic motion can in many ways make the nuclear wobbling mode much richer. The presence of aligned particles favours a particular (triaxial) shape and produces a unique pattern of electromagnetic transitions between the bands.

In the present work the detailed properties of the decay transitions between the bands determined from the analysis of experimental data are presented. Part of the results was published previously in Ref. [11]. The comparison between those properties and what is expected from the wobbling mode with aligned particles provides a firm evidence for the wobbling motion in ^{163}Lu with the excitation of one [11], and possibly two wobbling phonons.

We emphasize that the present exotic excitation mode uniquely related to triaxiality exists together with well developed band structures built on quasiparticle excitations in the normal deformed minimum. The ND and TSD structures are found at comparable energies for spins $I \leq 40$, while at the highest spin values reached the TSD structures are favoured.

2. Experimental methods and analysis

In an early Euroball [12] experiment on $^{163,164}\text{Lu}$ at Legnaro, an excited band (TSD2) with similar properties as the previously known band was observed in ^{163}Lu [13]. This band could not be connected to the rest of the level scheme, although it could be seen in coincidence with the known $\pi i_{13/2}$ band (TSD1) [1]. Carrying about 3% of the intensity in the reaction channel, as compared to the 10% of TSD1, this band was considered to be a candidate for a wobbling excitation built on TSD1.

To find the transitions that connect TSD2 to TSD1, a new experiment with the $^{139}\text{La}(^{29}\text{Si}, 5n)^{163}\text{Lu}$ reaction at a beam energy of 152 MeV, was done with the Euroball IV set-up [12] at Strasbourg. At the time, 15 Cluster detectors, 25 Clover detectors, and 26 Tapered detectors were used together with the BGO inner ball. With the gating conditions of 3 or more suppressed γ -rays in the Ge detectors and 8 or more γ -rays detected in the BGO inner ball, approximately 2.4×10^9 clean events were collected.

The data were sorted into 3- and 4-dimensional coincidence matrices and analysed with programs from the Radware package [14]. Furthermore, the events were stored in a database prepared for the “filtering technique” analysis [15], a new method with improved sensitivity for the extraction of weakly populated structures from high-fold events. The filtering technique gave hints of new excited TSD bands decaying into TSD1. They could be confirmed and further developed in the conventional 3D-cube analysis.

The multipolarity of the strongest established transitions connecting the excited TSD bands to TSD1 was determined from directional correlation of γ -rays from the oriented states (DCO-ratios) by using “25°” and “90°” data sorted into a “90° \times 25°” matrix. The two most forward rings of the Tapered detectors and the most backward ring of the Cluster detectors were included at “25°”, while the Clover detectors comprise the “90°” data. In addition, angular distribution ratios were extracted from two angular distribution matrices (“All \times 90°” and “All \times 25°”). For a determination of the spin alignment a “25° \times 25°” matrix was also sorted. Linear polarization measurements were obtained using vertical and horizontal scattering information from the two “90°” rings of Clover detectors. The linear polarization is extracted as

$$P = \frac{P_{\text{vert}} - P_{\text{horiz}}}{P_{\text{vert}} + P_{\text{horiz}}}.$$

In all matrices the data were selected by clean gates in TSD1 at any angle in the spin range 21/2–45/2 \hbar .

The spin alignment, usually parametrised as σ/I for a Gaussian distribution of the m -substate population, $P_m(I) \propto \exp(-\frac{m^2}{2\sigma(I)^2})$ [16], was determined from a comparison of the distribution ratio $W(\text{“25°”})/W(\text{“90°”})$ to the correlation ratio $W(\text{“25°”} \times \text{“25°”})/W(\text{“90°”} \times \text{“25°”})$, in which the experimental detection efficiencies cancel. The comparison was made for a number of stretched electric quadrupole ($E2$) transitions in TSD1 in the same spin region (29/2–63/2 \hbar) as the connecting transitions. There was no detectable spin dependence, and the average value of σ/I is 0.25 ± 0.02 . The calculated relation based on the relevant detector angles is shown together with the data in Fig. 3.

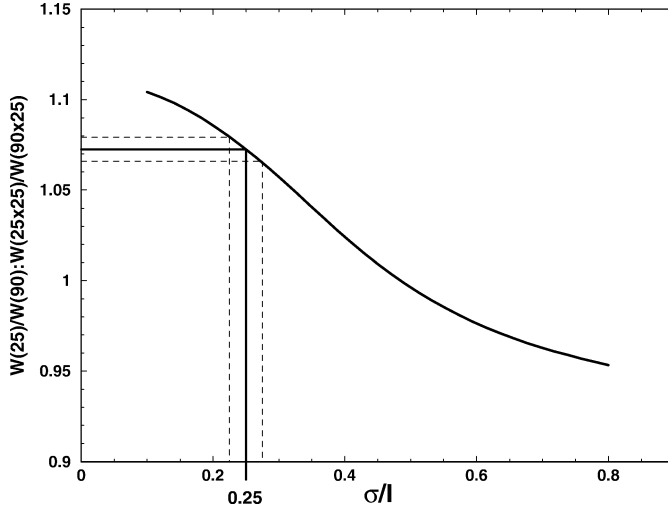


Fig. 3. Illustration of the determination of the spin alignment, σ/I , for an average of stretched $E2$ transitions in the spin range $29/2$ – $61/2\hbar$.

3. Results

The level scheme constructed on the basis of the coincidence relationships obtained from the analysis described above is presented in two parts, Figs. 4 and 5, covering the normal deformed and triaxial superdeformed structures separately. A listing of energies and relative intensities as obtained from the fits to the counts in the cubes [14] is given for the normal deformed and triaxial superdeformed band structures separately in Tables A1 and A2, respectively, of the Appendix. Branching ratios were obtained from gates set above the level of interest.

3.1. Normal deformed band structures

The known bands [1,13] built on the $[523]7/2^-$, $[404]7/2^+$ and $[411]1/2^+$ Nilsson orbitals have been extended. The $[402]5/2^+$ band of which only three levels were suggested in [13] has been fully developed up to the first expected band crossing. The three bands with positive parity are quite close in energy and apparently mixed at low spin, where several interconnecting M1 transitions are observed. In addition, two new coupled bands, X1 and X2, have been established. Spectra illustrating the coincidence relationships within these bands are found in Fig. 6.

For band X1, the decay pattern does not allow an unambiguous spin and parity determination. It is not possible to determine DCO ratios for the decay transitions due either to lack of statistics or because of contaminating transitions. Increasing the spin by one unit compared to the values shown in Fig. 4 would make the band X1 yrast, which is incompatible with its weaker population. Decreasing the spin one unit causes the decay transitions of 988.6, 1027.1, 1012.2 and 996.4 keV to be of $I \rightarrow I - 1$ character. This is possible, and would most likely imply positive parity since in the case of negative parity the

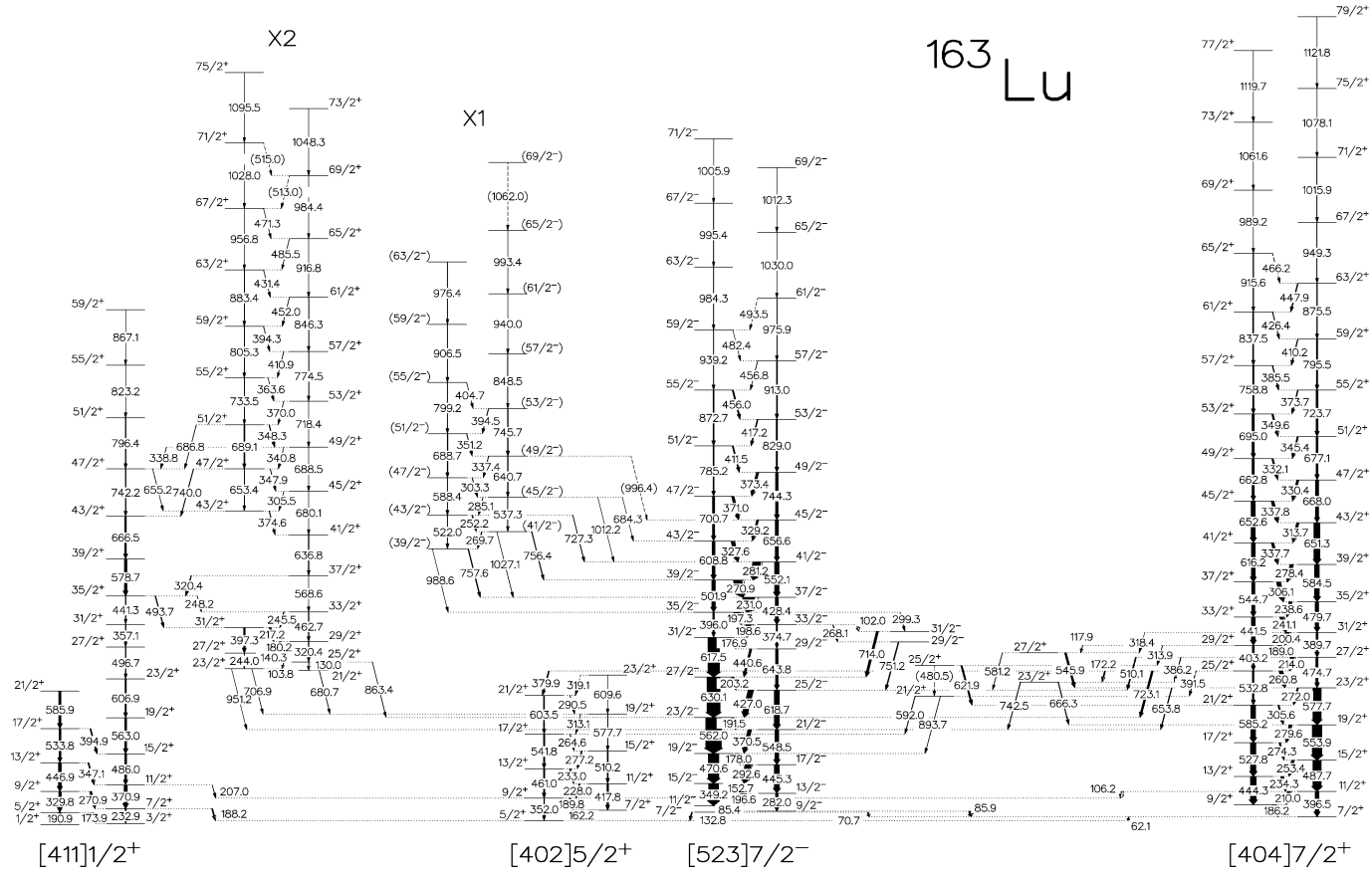


Fig. 4. Level scheme of normal deformed band structures in ^{163}Lu . The bands are labeled with Nilsson quantum numbers when these could be assigned. The new bands are labeled X1 and X2.

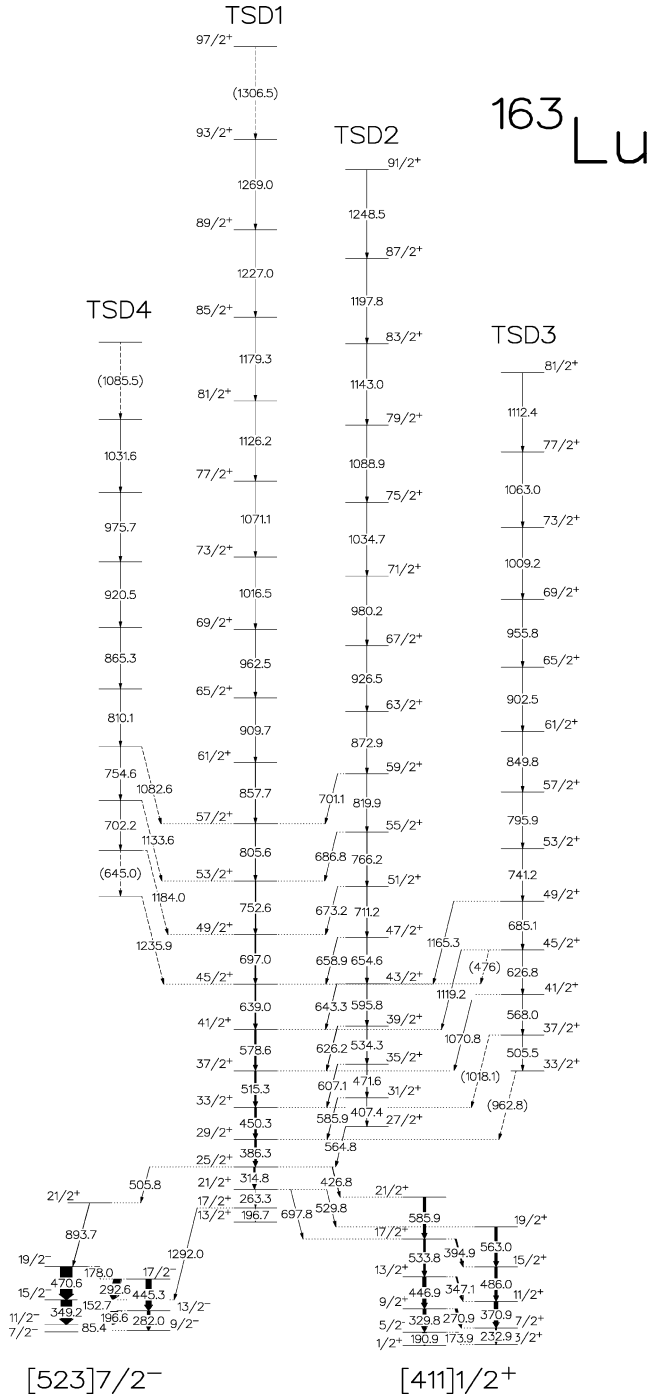


Fig. 5. Level scheme of triaxial SD band structures TSD1–TSD4, together with the ND structures populated in the decay of TSD1.

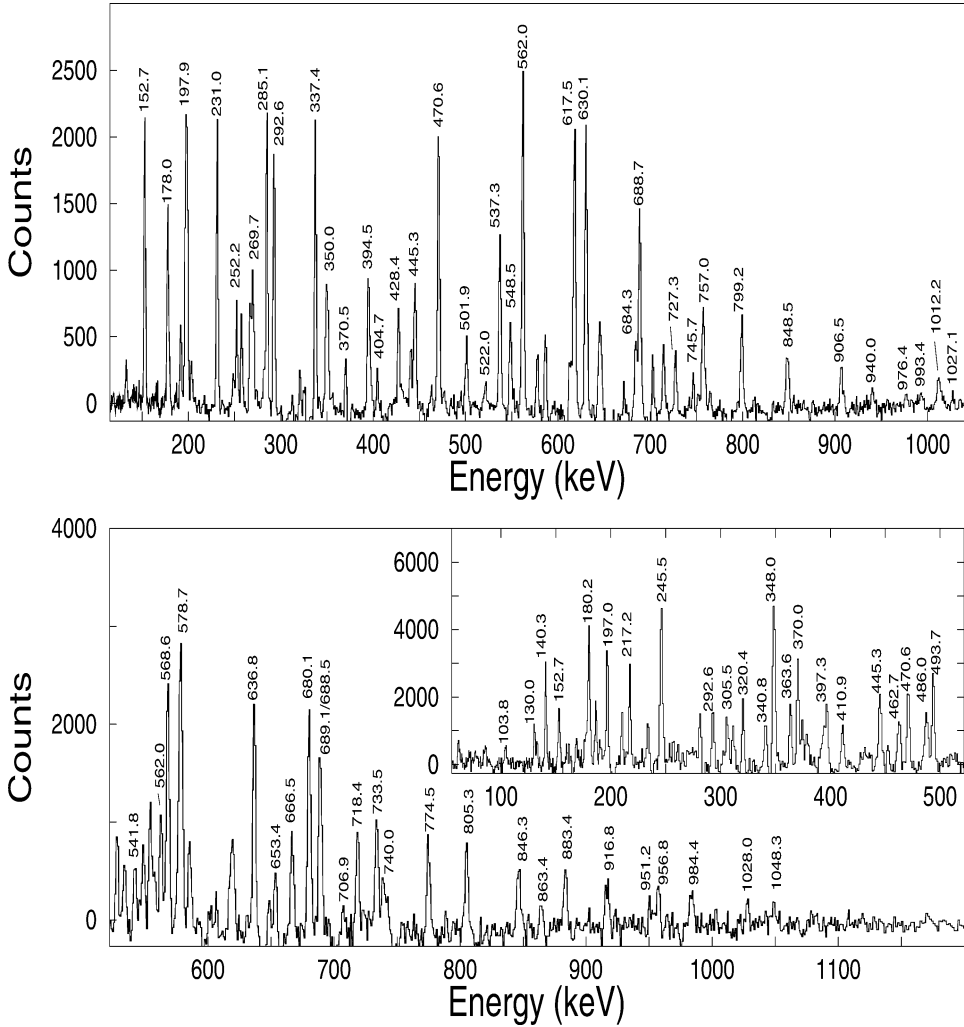


Fig. 6. Spectra documenting the coincidence relationship for the new ND bands. Top: X1, double gate on the 197 keV (multiple) transition in the $[523]7/2^-$ band and the 303.3 keV transition in band X1. Bottom: X2, double gate on a sum of the 140.3, 180.2 and 217.2 keV M1 transitions and a sum of all E2 transitions above $I = 41/2\hbar$ in band X2. The inset shows the lowest energy part of the spectrum.

$I \rightarrow I - 2$ decays, expected to compete due to higher transition energies, are unobserved. The spin and parity shown (in parenthesis) are the most likely values, but $37/2^+$ or, less likely, $37/2^-$ cannot be excluded for the lowest state.

The spin, and positive parity of the new coupled band, X2, is firmly established through its cross connection with the $[411]1/2^+$ band at spins $I \sim 35/2\hbar$ and $\sim 47/2\hbar$. At the lowest level the band X2 decays to the $[402]5/2^+$ band, and to the $[523]7/2^-$ band. With the spin and parity determined from the interaction with the $[411]1/2^+$ band, the decay transitions to the $[523]7/2^-$ band are of E1 character.

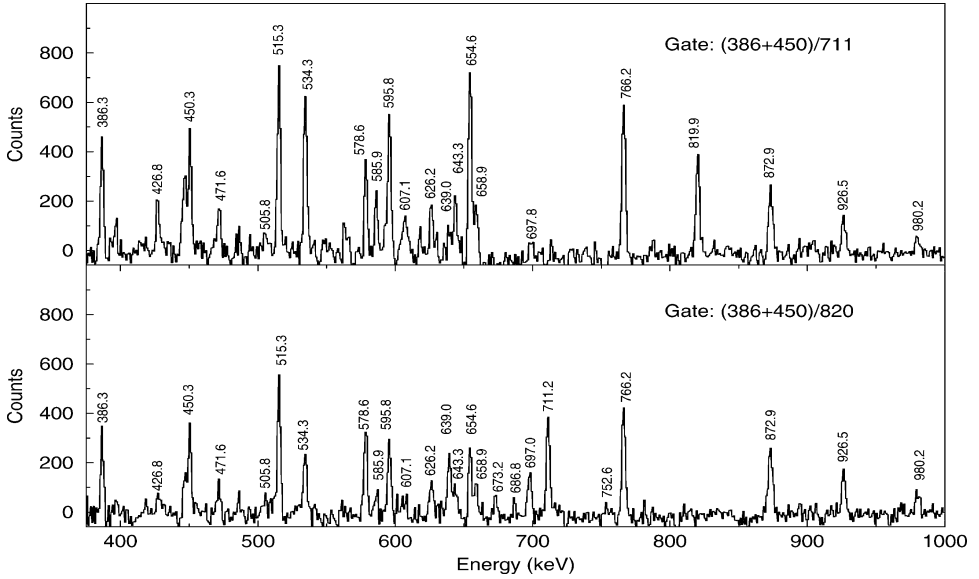


Fig. 7. Spectra documenting the coincidence relationship for the bands TSD1 and TSD2, as well as the transitions from TSD2 to TSD1.

3.2. Triaxial superdeformed band structures

In addition to extending the known band, TSD1, interpreted in Ref. [2] as an $i_{13/2}$ proton excitation in the strongly deformed triaxial minimum, most likely with positive γ , the weaker band, TSD2, found in our first Euroball experiment [13] has been extended to both higher and lower spin. Most importantly, TSD2 could be firmly connected to TSD1 by 9 transitions. Some of these connections are documented in the spectra shown in Fig. 7. Furthermore, two new excited TSD bands, TSD3 and TSD4, were also found to decay into TSD1 using a combination of the filtering technique [15] and cube analysis. The former method implied analysis of 2D matrices based on a filter including transitions in TSD1 in the range $21/2 \leq 57/2\hbar$. With gates on transitions in TSD3 and TSD4 a few candidates for decay out from both bands were found. For TSD3, the decay to TSD1 is established through 3 firmly and 2 tentatively placed transitions which is illustrated by spectra from (summed) double gates in the cube in Fig. 8. The connections from the new band, TSD4, to TSD1 are tentative.

Our emphasis has been to determine spin and parity of the two excited bands, TSD2 and TSD3, which are likely candidates for assignment as wobbling phonon excitations built on TSD1, and to measure the electromagnetic properties of the connecting transitions. Therefore, the angular distribution, DCO ratios and linear polarization of the connecting transitions have been analysed. As an example, the angular distribution for transitions connecting TSD2 to TSD1 is shown in Fig. 9, strongly favouring 90° .

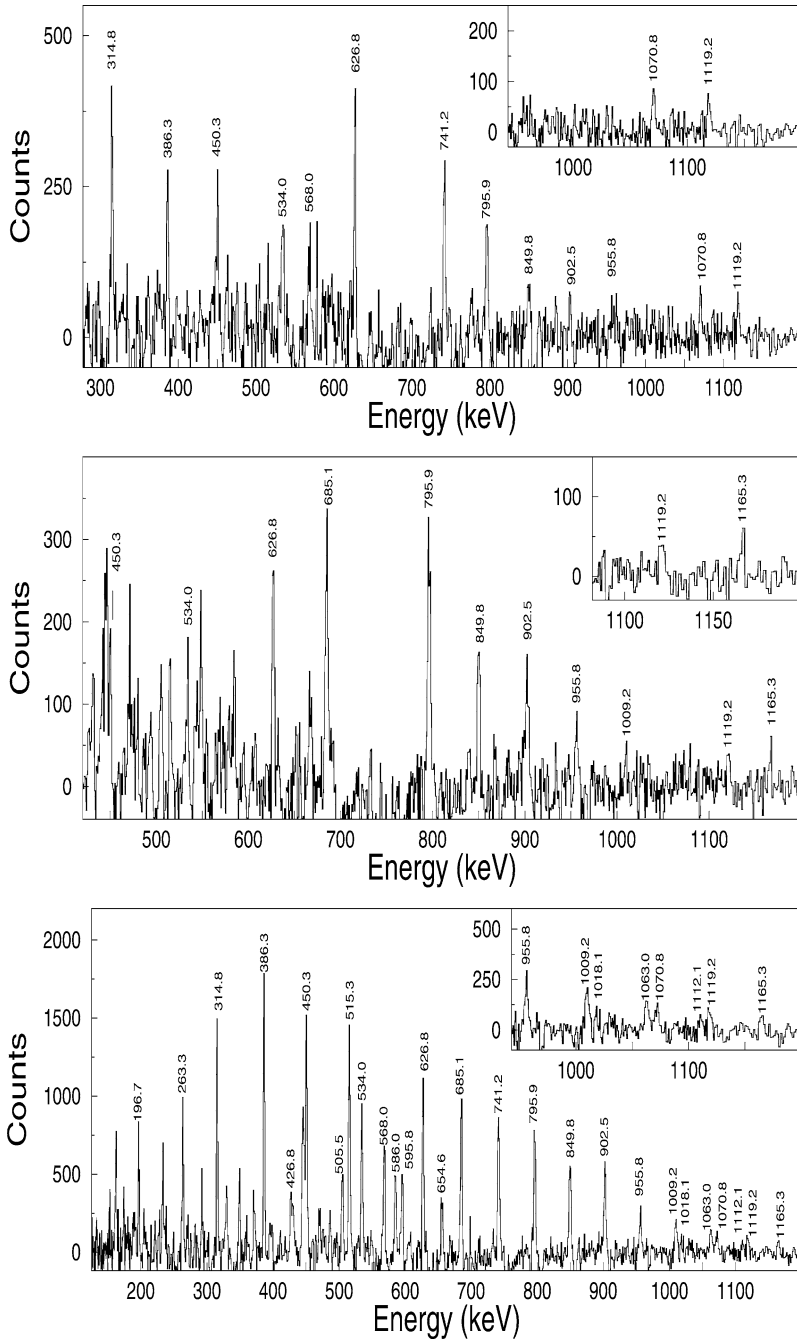


Fig. 8. Spectra documenting TSD3. Insets show parts of the highest energy region of the spectra enlarged. Double gate on a sum of the 386.3, 450.3 and 515.3 keV transitions in TSD1 and the 685 keV (top), the 741.2 keV (mid) and a sum of the 685.1, 741.2, 795.9 and 849.8 keV transitions in TSD3 (bottom), respectively.

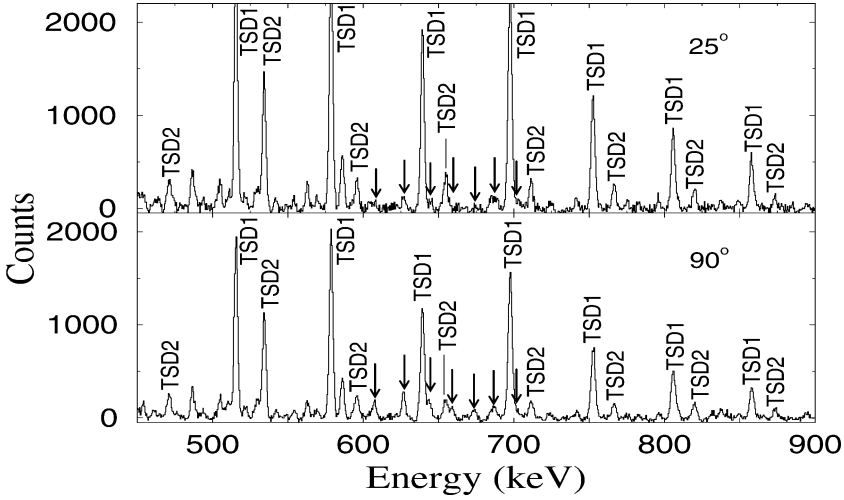


Fig. 9. Spectra from the angular distribution matrices gated on the 450 keV transition in TSD1. Connecting transitions are marked by arrows. Most other transitions are related to the decay of TSD1.

Table 1

Experimental values of angular distribution ratios, $W(25^\circ)/W(90^\circ)$, DCO ratios and polarization ($P = \frac{P_{\text{vert}} - P_{\text{horiz}}}{P_{\text{vert}} + P_{\text{horiz}}}$). The polarization obtained as an average for known stretched E2 and stretched M1 transitions are $+0.11(3)$ and $-0.11(5)$, respectively

E_γ (keV)	$J_i^\pi \rightarrow J_f^\pi$	$W(25^\circ)/W(90^\circ)$	DCO-ratio	Polarization
<i>TSD2</i> \rightarrow <i>TSD1</i> :				
607.1	$\frac{35}{2}^+ \rightarrow \frac{33}{2}^+$	0.42(2)	0.34(6)	0.05(5)
626.3	$\frac{39}{2}^+ \rightarrow \frac{37}{2}^+$	0.47(2)	0.33(6)	0.12(5)
643.3	$\frac{43}{2}^+ \rightarrow \frac{41}{2}^+$		0.32(6)	0.11(5)
658.9	$\frac{47}{2}^+ \rightarrow \frac{45}{2}^+$	0.47(2)	0.30(6)	0.17(9)
673.2	$\frac{51}{2}^+ \rightarrow \frac{49}{2}^+$	0.46(2)	0.38(6)	0.18(9)
<i>TSD3</i> \rightarrow <i>TSD1</i> :				
1119.2	$\frac{45}{2}^+ \rightarrow \frac{41}{2}^+$	1.45(10)		
1165.3	$\frac{49}{2}^+ \rightarrow \frac{45}{2}^+$	1.47(9)	1.05(20)	

With the measured spin alignment, $\sigma/I = 0.25 \pm 0.02$, the results of the angular correlation and angular distribution analyses exclude the possibility of pure transitions of stretched dipole or nonstretched quadrupole nature and imply that the transitions connecting TSD2 to TSD1 are of mixed electric and magnetic nature with $\Delta I = 1$. Results of the angular distribution ratio, the DCO ratio and polarization analyses are given in Table 1.

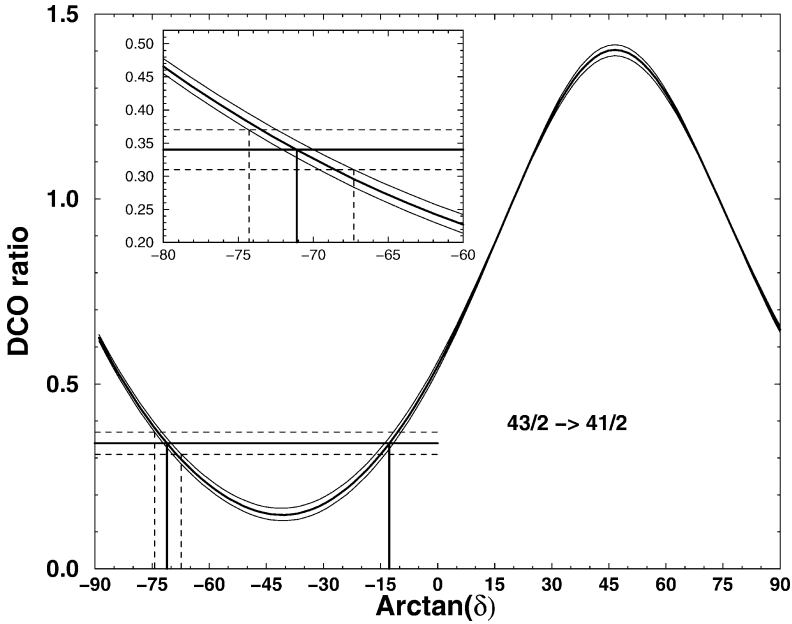


Fig. 10. Determination of the mixing ratio, δ , of the average of the DCO ratios for the transitions connecting TSD2 to TSD1, given in Table 1. The inset shows an enlarged region around $\text{Arctan}(\delta) = -70^\circ$.

The mixing ratio δ of the electric quadrupole and magnetic dipole transition strength $E2/M1$ has been determined for the strongest of the transitions connecting TSD2 to TSD1 using both angular distribution ratio and DCO ratio analyses. With no spin dependence within the errors in both types of ratios (see Table 1), these were averaged over the different transitions, and a value of δ corresponding to the average value determined from both methods, as illustrated for the DCO ratio analysis in Fig. 10. The results from both methods are combined to give two possible final values of $\delta = -3.10^{+0.36}_{-0.44}$ or $-0.22^{+0.05}_{-0.03}$.

In the polarization measurements the connecting transitions show their electric character, with the same sign and magnitude as the neighbouring stretched $E2$ in-band transitions, thus excluding the latter solution of $\delta = -0.22^{+0.05}_{-0.03}$. The final result with $\delta = -3.10^{+0.36}_{-0.44}$ corresponds to $(90.6 \pm 1.3)\%$ $E2$ and $(9.4 \pm 1.3)\%$ $M1$ in the connecting transitions, when disregarding the alternative solution of $M2/E1$ mixing which would result in unexpectedly large matrix elements for both $M2$ and $E1$ transitions.

Based on the consistently similar values of the mixing ratios, δ , obtained for the transitions connecting TSD2 to TSD1 and their electrical character, the spin and parity of TSD2 are unambiguously determined, in accordance with the level scheme in Fig. 5.

The angular distribution ratio and DCO ratio analyses give confidence in assigning stretched $E2$ character to the transitions connecting TSD3 to TSD1 in accordance with the

spin and parity shown in Fig. 5. This conclusion agrees with the result of the polarization analysis although the errors here are quite large.

For the weakest populated band, TSD4, no spin and parity can be assigned.

4. Discussion of experimental band structures

4.1. Properties of the ND band structures

In the interpretation of the new bands and of the high frequency properties of the $[404]7/2^+$ band, alignments, crossing frequencies as well as experimental estimates of $B(M1)/B(E2)$ values have been utilized. Experimental relative alignments are shown in Fig. 11 for the ND bands, except for band X1 and the excitation energy relative to a rigid reference is shown in Fig. 12 for the same ND bands.

4.1.1. Expected crossing frequencies

The first $i_{13/2}$ neutron crossing denoted (AB) is expected to occur in all the one-quasiproton excitations at the same frequency, $\hbar\omega \sim 0.26$ MeV, as found in the even-even neighbours, ^{162}Yb and ^{164}Hf [17].

A second $i_{13/2}$ neutron crossing, denoted (BC), will be present in two-quasineutron excitations in which the A quasineutron is involved. The lowest negative-parity neutron Nilsson orbital in these nuclei is $[521]3/2^-$, found in ^{161}Yb and in ^{163}Yb [17]. In ^{163}Yb the $[523]5/2^-$ orbital is almost as low in energy [17]. The quasiparticles with $\alpha = +1/2, -1/2$

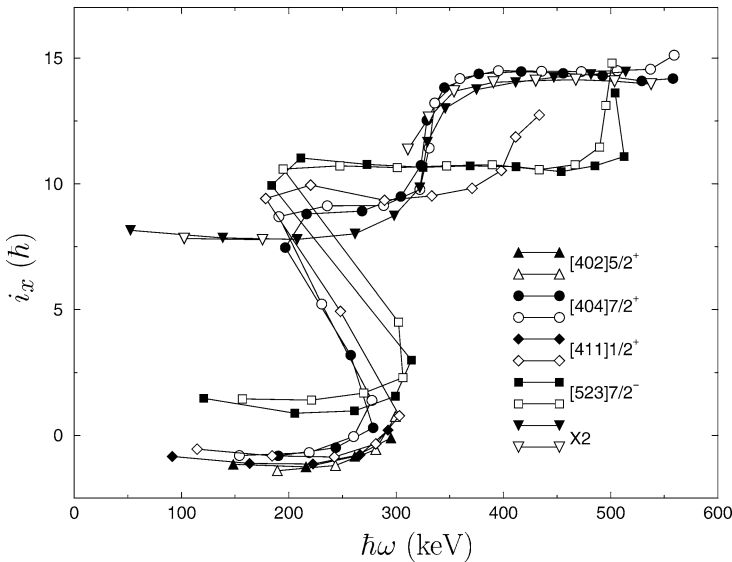


Fig. 11. Alignment of all ND bands except X1, relative to a reference, $I_{\text{ref}} = \mathfrak{S}_0\omega + \mathfrak{S}_1\omega^3$ with $\mathfrak{S}_0 = 30\hbar^2 \text{ MeV}^{-1}$ and $\mathfrak{S}_1 = 40\hbar^4 \text{ MeV}^{-3}$. K -values are used according to the Nilsson labels and for Band X2, $K = 15/2$ is used.

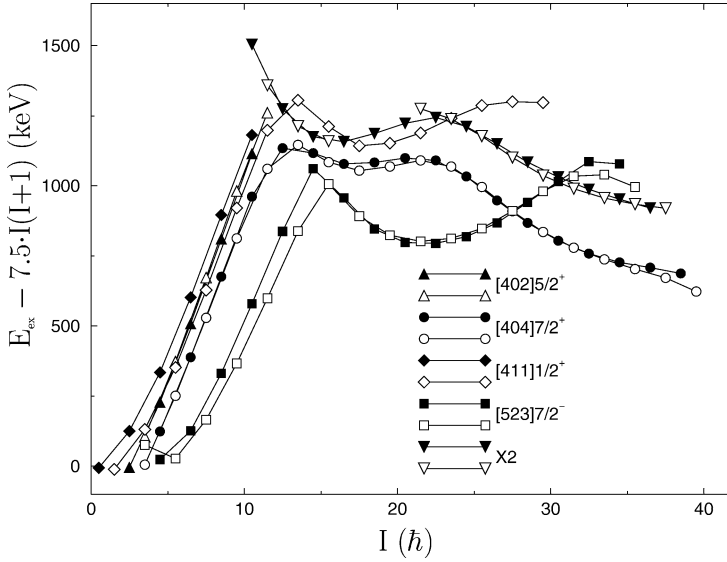


Fig. 12. Excitation energy, less a rigid reference, vs I , for all ND bands except X1.

related to these 2 negative parity Nilsson orbitals, $[521]3/2^-$ and $[523]5/2^-$, are denoted by E,F and G,H, respectively. In the negative parity bands built on the $[642]5/2^+ \otimes [521]3/2^-$ two-quasineutron configuration, AE, in ^{162}Yb and ^{164}Hf [17] the BC crossing occurs at $\hbar\omega \sim 0.32$ MeV. Since the AE band in both these nuclei appears quite low in excitation it is expected that three-quasiparticle bands in which a quasiproton is coupled to the AE quasineutrons are found in odd- Z nuclei, and many such examples are known, for example in ^{165}Lu [3].

The lowest proton crossing, presumably caused by the alignment of a pair of $h_{11/2}$ quasiprotons is found in several bands in $^{161,162}\text{Yb}$ and in $^{164,165}\text{Hf}$ at a frequency, $\hbar\omega$, varying from 0.42 to 0.46 MeV [17]. A second proton alignment is present in ^{161}Yb at $\hbar\omega \sim 0.58$ MeV, possibly caused by a mixed crossing in which the strongly aligned proton $h_{9/2}$ $[541]1/2^-$ orbital is involved.

4.2. Assigned ND band structures

4.2.1. The $[402]5/2^+$ and $[411]1/2^+$ bands

The $[402]5/2^+$ band is established up to the frequency of the AB crossing. For the $[411]1/2^+$ band the negative signature partner is extended sufficiently high in spin to reveal both the AB crossing at $\hbar\omega \sim 0.26$ MeV and the first $h_{11/2}$ proton crossing as an upbend at $\hbar\omega \sim 0.42$ MeV.

4.2.2. The $[404]7/2^+$ band

The $[404]7/2^+$ band appears to have both signatures well established quite high in spin and the first crossing, (AB), is observed as expected. Levels representing extensions of the crossing bands are observed for spins $21/2^+ \hbar$, $25/2^+ \hbar$ and $23/2^+ \hbar$, $27/2^+ \hbar$ in the

negative and positive signature partner, respectively. A second crossing occurs at $\hbar\omega \sim 0.32$ MeV. This is the frequency of the second $i_{13/2}$ neutron crossing, (BC), which of course is blocked in the $[404]7/2^+$ band above the frequency of the (AB) crossing. We suggest that above the (AB) crossing the $[404]7/2^+$ band has changed its character into a three-quasiparticle band, based on the $[523]7/2^-$ proton coupled to AE. A similar three-quasiparticle band is observed to strongly mix into the $[404]7/2^+$ band in ^{165}Lu around the AB crossing [3]. This suggested three-quasiparticle character explains the observed (BC) crossing, and it also explains the observed increase in $B(M1)/B(E2)$ values from ~ 1 to $\sim 1.4\mu_N^2/e^2b^2$ at this crossing (see Table A1), in contrast to the expected drastic decrease if the crossing was due to the alignment of a pair of $h_{11/2}$ protons in the $[404]7/2^+$ band with the AB neutrons aligned, as suggested in Ref. [1]. The measured values of $B(M1)/B(E2)$ in this region are also in better agreement with the expectations for the suggested three-quasiparticle band.

4.2.3. The band X2

The negative signature partner of band X2 interacts with the $[411]1/2^+$ band at two spin values which apparently disturbs the in-band decay pattern and causes the mixing of some levels at medium spin. The band has a large alignment which implies three-quasiparticle nature at low spin and an alignment gain of very similar nature as observed for the three-quasiparticle band, $\pi[523]7/2^- \otimes \nu AE$, into which the $[404]7/2^+$ band is suggested to develop above the AB crossing. The band X2 is naturally interpreted as a three-quasiparticle band based on the $[523]7/2^-$ proton coupled to the AG two-quasineutron configuration. The values of $B(M1)/B(E2)$ are ~ 1.4 and $1.8\mu_N^2/e^2b^2$, respectively, for the extended $[404]7/2^+$ band and X2 in the spin range $I \sim 22\text{--}30\hbar$, which agrees with the relative expectations for the two 3-quasiparticle structures suggested.

4.2.4. The $[523]7/2^-$ band

The $[523]7/2^-$ band has no alignment gain in a large range from the regular AB crossing at $\hbar\omega \sim 0.26$ MeV up to $\hbar\omega \sim 0.49$ MeV, the first $h_{11/2}$ crossing at $\hbar\omega \sim 0.41$ MeV being blocked. For bands in which the $[523]7/2^-$ orbital is involved the second $h_{11/2}$ crossing will be expected earliest in the negative signature whereas in the positive signature a change of character to the strongly aligned positive signature partner of the $h_{9/2}[541]1/2^-$ orbital may take place at a close, higher frequency. The present data agree with this expectation but do not allow a further investigation of these high-frequency crossings.

4.2.5. The band X1

The band X1 exhibits no crossings. Since its spin and parity are not firmly assigned it is difficult to suggest possible configurations. The fairly large values of $B(M1)/B(E2) \sim 1.4\mu_N^2/e^2b^2$ in the spin range $I \sim 22\text{--}28\hbar$ could point in the direction of the $[402]5/2^+$ band above the AB crossing, if the band has positive parity.

4.3. Properties of the TSD bands

The three excited TSD bands all decay into TSD1. For the connection between TSD2 and TSD1 only $\Delta I = -1$ transitions are established. The $\Delta I = +1$ transition have very low energy and could not be observed. The possible $\Delta I = -1$ transitions from TSD3 to TSD2 have energies in the range 400–500 keV. Due to unfavourable gating conditions none of these transitions could be determined, except for an upper limit for $I = 45/2\hbar$. The electromagnetic properties of some of the connecting transitions from TSD2 (mixed E2/M1) and TSD3 (stretched E2) have been determined. It is therefore possible to extract values for $B(E2)_{\text{out}}/B(E2)_{\text{in}}$ for the transitions from both bands and $B(M1)/B(E2)_{\text{in}}$ for the transitions from TSD2. They are important observables to be compared to theoretical values from the calculations described in Section 5.

The TSD bands are all characterized by very similar dynamic moments of inertia, $\mathfrak{J}^{(2)}$. Since this quantity is independent of spin it can be presented for all 4 bands as shown in the bottom part of Fig. 13. The moment of inertia increases gradually from ~ 60 to $\sim 75\hbar^2 \text{ MeV}^{-1}$ over the spin region shown in the figure, and at the highest frequency above $\sim 0.6 \text{ MeV}$ a steeper rise is observed in TSD1 and TSD2, both established this high in frequency. When looking closer into details, it appears that $\mathfrak{J}^{(2)}$ of TSD4 is about 5% smaller than the average value of $\mathfrak{J}^{(2)}$ for the three other bands which have almost identical dynamic moments of inertia. It can be noted that the ND bands in regions avoiding crossings have values considerably lower [5,11,13].

It is also interesting to investigate the relative alignment of TSD1-3, shown in the top part of Fig. 13. Relative to the reference chosen they all show a gradual alignment gain up to $\hbar\omega \sim 0.5 \text{ MeV}$, a flat part and at the highest frequencies an upbend starts to develop. The

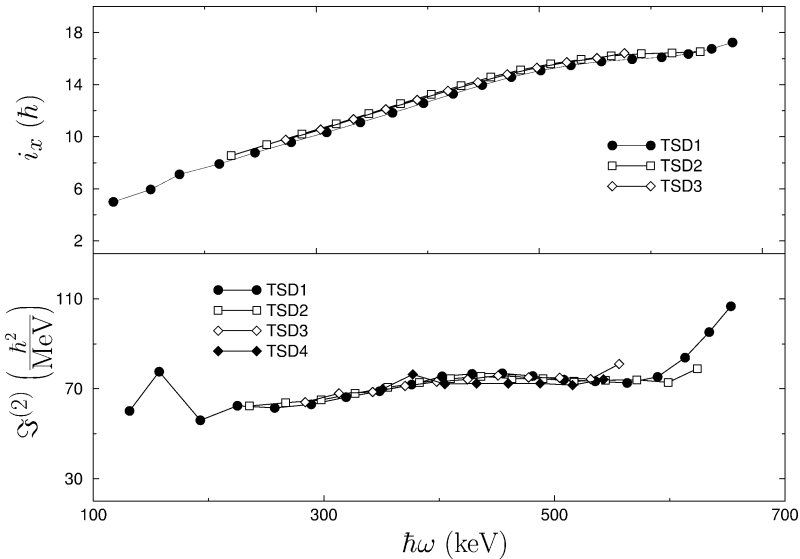


Fig. 13. Alignment relative to a reference, $I_{\text{ref}} = \mathfrak{J}_0\omega + \mathfrak{J}_1\omega^3$ with $\mathfrak{J}_0 = 30\hbar^2 \text{ MeV}^{-1}$ and $\mathfrak{J}_1 = 40\hbar^4 \text{ MeV}^{-3}$ (top) and dynamic moment of inertia (bottom) for bands TSD1-3.

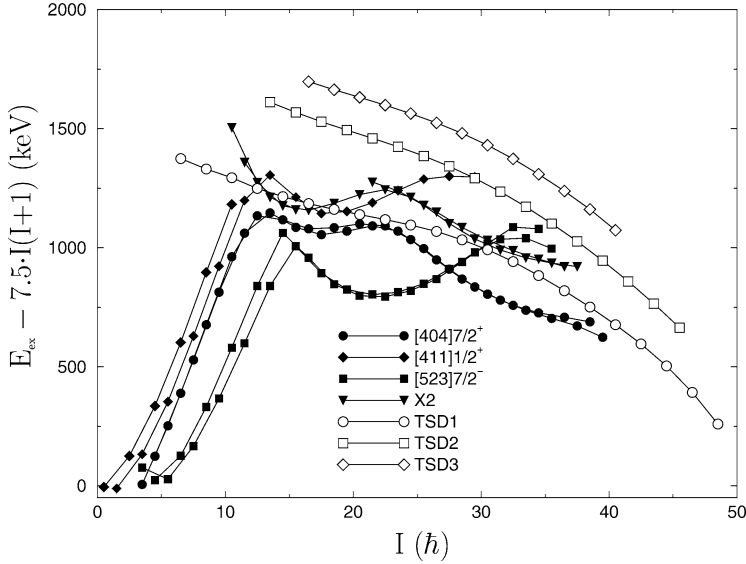


Fig. 14. Excitation energy minus a rigid reference for all bands in ^{163}Lu , except X1 and TSD4, for which no firm spin could be assigned. ND bands are shown with filled and TSD bands with open symbols.

alignment for TSD2 and TSD3 are almost identical and about $0.5 \hbar$ larger than for TSD1 for the full range measured. Here we have adopted the way of extracting the alignment analogous to that used for the axially symmetric shape.

With the very similar alignments and dynamic moments of inertia it is natural to suggest that all of the bands, TSD1-3, have similar intrinsic structure. We can therefore assume that they belong to the same local potential energy minimum, which according to the UC cranking calculations is lowest for positive value of γ . In Fig. 14 the excitation energies of these three TSD bands are compared to the ND band structures (except for X1 which has uncertain spin). Below $I = 40\hbar$ TSD1 and TSD2 both come very close to ND structures at several spin values. Yet the only connection found due to interactions is the decay from TSD1 to the $[411]1/2^+$ band around $I = 21/2\hbar$ [13]. The present experiment revealed a weak decay to a $I^\pi = 21/2^+\hbar$ state interpreted as a low spin extension of the $[404]7/2^+(\text{AB})$ band which presumably mixes into the $[411]1/2^+$ band at this spin.

4.3.1. Possible interpretations of TSD2 and TSD3

Both TSD2 and TSD3 have positive parity. TSD2 has signature $\alpha = -1/2$ while TSD3 has signature $\alpha = +1/2$ like that of the known favoured signature of the $\pi i_{13/2}$ orbital, TSD1. We discuss a few possibilities which provide interpretations alternative to the wobbling phonon excitations built on TSD1 which is analysed in Section 5 below.

The UC cranking model calculations predict a large signature splitting ($\gtrsim 1 \text{ MeV}$) of the $\pi i_{13/2}$ orbital in the triaxial minimum with positive γ . Furthermore, the local minimum associated with the unfavoured signature in the proton system is found at

a smaller quadrupole deformation, $\varepsilon_2 \sim 0.32$ and a larger triaxiality, $\gamma \sim 40^\circ$. This highly excited signature partner therefore has features qualitatively different from TSD1, unlike those of TSD2. Another possible configuration with $(\pi, \alpha) = (+, -1/2)$ may be composed by $\alpha = +1/2$ in the proton system, like TSD1, and a two-quasineutron excitation with $(\pi, \alpha) = (+, 1)$. Such configurations are predicted by the UC calculations to have similar local minima as TSD1, but the lowest band structure of this kind is expected at approximately the same excitation energy as the signature partner, and therefore also considerably higher than measured.

A possible configuration for TSD3 could also be one with $\alpha = +1/2$ in the proton system, like TSD1, and a two-quasineutron excitation with $(\pi, \alpha) = (+, 0)$, different from the lowest pair of $i_{13/2}$ quasineutrons most likely responsible for the gradual alignment gain observed in all three TSD bands. The lowest configuration of this kind is also expected higher in excitation relative to TSD1 than observed.

5. Nuclear wobbling motion with aligned particles

As described in the introduction, in the wobbling motion of quantum mechanical systems described in the literature [10] the only angular momentum considered in the motion is the total angular momentum I . However, in the wobbling motion of nuclei the angular momentum coming from the intrinsic motion can also play a role. In the understanding of the experimental data on the SD rotational bands in ^{163}Lu the presence of a high- j aligned particle plays a crucial role in the wobbling motion [11]. The wobbling motion is strongly related to the shell-structure of the nucleus and can appear at relatively low angular momenta. Moreover, the nuclear shell-structure favours a particular (triaxial) shape depending on angular momenta as well as the neutron and proton number.

In the region near the yrast line almost all the excitation energy is tied up in the single degree of freedom associated with the rotation. The nucleus is therefore cold, and high- j one-particle orbitals have played a special role in the yrast spectroscopy. The rotational perturbation in the particles occupying those orbitals is so strong that the angular momentum of those particles immediately aligns as rotation sets in. It is known that corresponding to the degree of shell-filling a particular triaxial shape (a particular value of γ) is favoured by the fully aligned high- j particle.

In the following we consider the intrinsic Hamiltonian

$$H_{\text{intr}} = \sum_v (\epsilon_v - \lambda) a_v^\dagger a_v + \frac{\Delta}{2} \sum_{\mu, \nu} \delta(\bar{\mu}, \nu) (a_\mu^\dagger a_\nu^\dagger + a_\nu a_\mu) \quad (1)$$

where Δ is the pair-correlation parameter in the BCS approximation and ϵ_v expresses the one-particle energies for a potential V . For a single j -shell we can write the triaxially-deformed quadrupole potential in the form

$$V = \frac{\kappa}{j(j+1)} ((3j_3^2 - j(j+1)) \cos \gamma + \sqrt{3}(j_2^2 - j_1^2) \sin \gamma) \quad (2)$$

where κ , which is proportional to the size of the quadrupole deformation β_2 , is used as energy unit [18]. The cranking Hamiltonian is written as

$$H_{\text{CR}} = H_{\text{intr}} - \hbar\omega j_x \quad (3)$$

taking the x -axis as the cranking axis. It is shown [19] that for a given value of $(\lambda, \Delta, \omega)$ the quasiparticle energy of H_{CR} is a minimum for $j_x = j$ and the γ -value determined by

$$-2\cos(\gamma - 60^\circ) = \lambda/\kappa \quad \text{for } -2 < \lambda/\kappa < 2, \quad (4)$$

where λ expresses the degree of shell-filling. We note that all one-particle energy eigenvalues ϵ_v of the potential (2) for a single- j shell lie well inside the region of $-2 < (\epsilon_v/\kappa) < 2$. Examples given by the relation (4) are:

$$\gamma = \begin{cases} -30^\circ & \text{for } \lambda = 0, \\ 0 & \text{for } \lambda/\kappa = -1.0, \\ +20^\circ & \text{for } \lambda/\kappa = -1.532. \end{cases} \quad (5)$$

The half-filled shell, $\lambda = 0$, corresponds approximately to the case of $h_{11/2}$ protons in β -stable rare-earth nuclei, while $\lambda/\kappa = -1.532$ for $\gamma = +20^\circ$ expresses the Fermi level placed just below the lowest one-particle energy eigenvalue. The latter expresses the situation of $i_{13/2}$ protons for the SD bands of ^{163}Lu .

When a given γ value favoured by the aligned particle is supported also by the core particles, the nucleus may keep the shape in a wide region of angular momentum. In the favoured-signature (α_f) state with the fully aligned particle the rotation of the core about the axis of the largest moment of inertia for the shape given by Eq. (4) is energetically cheapest. If the triaxial shape is strongly favoured in energy by the fully aligned high- j particle, the unfavoured-signature (α_u) state, which consists of the fully aligned particle together with a wobbling motion of the rotational angular momentum of the core, may become very low in energy. When the gain in the intrinsic energy of the high- j particle configuration in the wobbling mode wins against the loss in the collective rotation energy of the core, the wobbling mode becomes the lowest α_u state. At very high spins the rotational energy dominates over the intrinsic energy and, thus, in the lowest α_u state the wobbling mode will be replaced by the cranking-like mode. The possibility of this kind of crossing of the two α_u bands along the yrast lines is pointed out in Ref. [20], taking an example of rotational bands based on $h_{11/2}$ protons in odd- Z β -stable rare-earth nuclei. The unsuccessful attempt of finding such experimental data might be due to the fact that the triaxial shape ($\gamma \approx -30^\circ$) favoured by the aligned $h_{11/2}$ proton was not supported by the core particles of those odd- Z nuclei in the relevant region of angular momentum.

We note that the wobbling motion cannot be described by the cranking model. Thus, as in Ref. [20], we solve the particle-rotor Hamiltonian

$$H_{\text{PR}} = H_{\text{intr}} + \sum_{k=1,2,3} \frac{\hbar^2}{2\mathfrak{I}_k} R_k \quad (6)$$

where $\vec{R} = \vec{I} - \vec{j}$ expresses the collective rotational angular momentum of the core. It is found that in the region of $N \sim 94$ and $Z \sim 71$ the “Ultimate Cranker” [3] predicts

stable triaxial shapes ($\gamma \sim \pm 20^\circ$) with large quadrupole deformation for all combinations of parity and signature and for the angular momenta relevant to the observed TSD bands in ^{163}Lu . Following the fact in (5) that $\gamma = +20^\circ$ is preferred by the fully aligned $j = i_{13/2}$ proton in ^{163}Lu , we perform the $i_{13/2}$ -particle-rotor calculation along the line of Ref. [20] with parameters $\gamma = +20^\circ$, $\Delta/\kappa = 0.30$, and $\kappa \mathfrak{I}_0 = 90$. The latter two parameters are chosen so that the observed level scheme of both TSD1 and TSD2 bands is, on the average, reproduced using a proper value of κ . Employment of the hydrodynamical moments of inertia

$$\mathfrak{I}_k = \frac{4}{3} \mathfrak{I}_0 \sin^2 \left(\gamma + \frac{2}{3} \pi k \right) \quad (7)$$

automatically restricts ourselves to the rotation with $-60^\circ < \gamma < 0^\circ$ in the sense of the cranking model. That is, the largest moment of inertia and, consequently, the largest component of collective rotational angular momentum is the one along the intermediate axis of the nuclear shape. In order to get a rotation in the particle-rotor model, which corresponds to $\gamma > 0$ in the cranking sense, we exchange [21] the moments of inertia, \mathfrak{I}_x and \mathfrak{I}_y , obtained from the hydrodynamical model. For example, $\kappa \mathfrak{I}_0 = 90$ with $\gamma = +20^\circ$ means $\kappa \mathfrak{I}_x = 116$, $\kappa \mathfrak{I}_y = 50$ and $\kappa \mathfrak{I}_z = 14$, so that the system rotates mainly about the x -axis, which is the shortest axis of the $|\gamma| = 20^\circ$ triaxial shape.

If we use the value of $\lambda/\kappa = -1.532$, which is most favourable for the fully aligned $i_{13/2}$ proton at $\gamma = +20^\circ$, the aligned $i_{13/2}$ particle coupled with the wobbling motion of the core remains the lowest α_u state in the entire region of the total angular momenta of TSD2, as discussed in the previous section. See Figs. 15 and 16. However, in order to illustrate

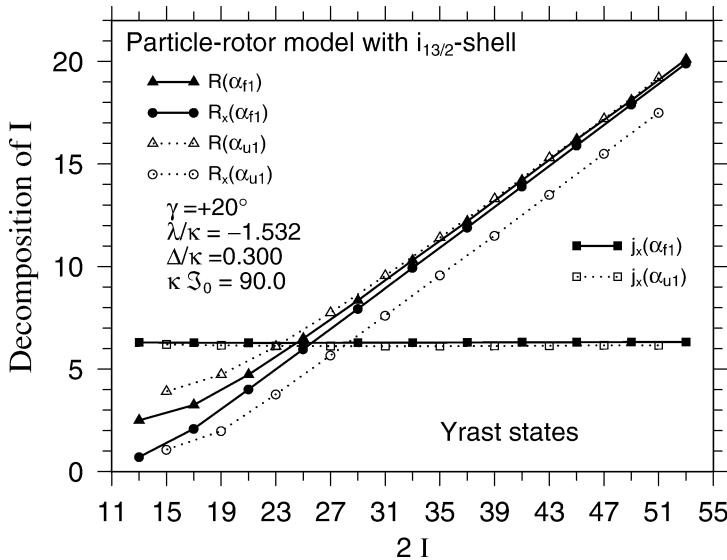


Fig. 15. Calculated values of R , R_x and j_x , which are defined by (8) using the wave functions of the lowest-lying α_{f1} and α_{u1} bands, as a function of the total angular momentum I . The shell-filling parameter used, $\lambda/\kappa = -1.532$, is the most favourable value for $\gamma = +20^\circ$.

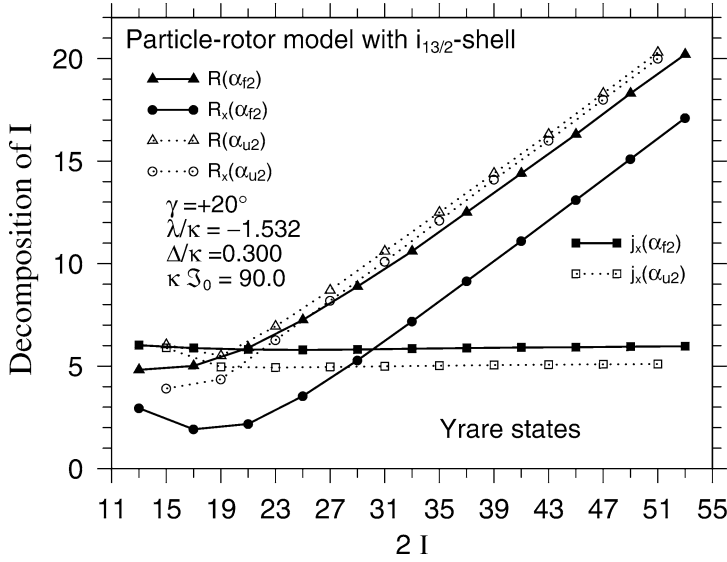


Fig. 16. Calculated values of R , R_x and j_x , which are defined by (8) using the wave functions of the second lowest-lying α_{f2} and α_{u2} bands, as a function of the total angular momentum I . Used parameters are the same as those in Fig. 15.

the band crossing of the “wobbling” regime and the “cranking” regime in the α_u states, in Fig. 17 we choose $\lambda/\kappa = -1.20$, for which the cranking regime becomes energetically lower than the wobbling regime at angular momentum considerably lower than in the case of $\lambda/\kappa = -1.532$. In Figs. 15–17 R , R_x and j_x defined by

$$\begin{aligned}
 R(R+1) &\equiv \langle R_x^2 \rangle + \langle R_y^2 \rangle + \langle R_z^2 \rangle, \\
 R_x &\equiv \sqrt{\langle R_x^2 \rangle}, \\
 j_x &\equiv \sqrt{\langle j_x^2 \rangle}
 \end{aligned} \tag{8}$$

are shown as a function of the total angular momentum, I . In the above expressions $\langle \rangle$ expresses the expectation values, which are calculated by using the wave functions obtained from the particle-rotor model. Both I and j are good quantum numbers in the present model, while R is not.

In Fig. 17 it is seen that for the yrast α_u ($= -1/2$) states where $I = \alpha \pmod{2}$, we have $j_x \approx j$ and $R_x \approx R - 2$ for $I < 35/2\hbar$; namely the intrinsic energy with the fully aligned $i_{13/2}$ proton is made to be lowest by the sacrifice of the core rotational energy. On the other hand, for $I > 35/2\hbar$ $j_x \approx j - 1$ and $R_x \approx R$; namely the core rotational energy is made to be lowest by the sacrifice of the intrinsic energy. In contrast, for the yrast α_f ($= +1/2$) states we have $j_x \approx j$ and $R_x \approx R$ for all I values, in which both the intrinsic (particle) angular momentum \vec{j} and the core angular momentum \vec{R} can take the respective lowest-energy configuration. An appropriate description is that for $I < 35/2\hbar$ the yrast α_u states are in the “wobbling” regime, while for $I > 35/2\hbar$ they are in the “cranking” regime. Though in the α_u band of the wobbling regime the alignment of the $i_{13/2}$ proton is nearly

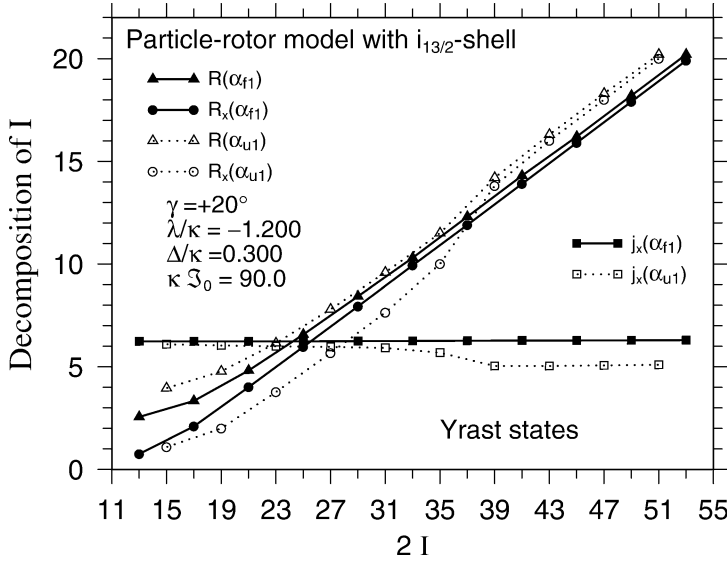


Fig. 17. Calculated values of R , R_x and j_x , which are defined by (8) using the wave functions of the lowest-lying states, as a function of the total angular momentum I . In order to illustrate the crossing of the α_u bands in the present region of angular momenta, the shell-filling parameter, $\lambda/\kappa = -1.20$, is used, which is not the most favourable value for $\gamma = +20^\circ$.

equal to that of the yrast α_f band, the signature splitting of the energy has the same sign as in the cranking regime.

Choosing the most favourable γ -value, $\gamma = +20^\circ$, for $\lambda/\kappa = -1.532$, in Fig. 15 (Fig. 16) we show the calculated values of R , R_x and j_x for the yrast (yrare) α_{f1} and α_{u1} (α_{f2} and α_{u2}) bands. In these figures the quantities of α_f (α_u) bands are denoted by filled (open) signs and are connected by solid (dotted) lines, in the way similar to Fig. 17. It is observed that $R_x \approx R$ for the α_{f1} and α_{u2} bands, while $R_x \approx R - 2$ for the α_{u1} and $R_x \approx R - 3.2$ for the α_{f2} band. For the α_{f1} , α_{u1} and α_{f2} bands we find $j_x \gtrsim 6$, while $j_x \approx 5$ for the α_{u2} band. The expectation values of the intrinsic Hamiltonian H_{intr} in the former three bands are comparable and considerably smaller than the one in the α_{u2} band. Based on these observations the α_{u1} and α_{f2} bands are classified as the wobbling modes, which are built on the α_{f1} band, having $n_w = 1$ and $n_w = 2$, respectively, where n_w expresses the wobbling phonon number [10] of the core. In contrast, the α_{u2} band belongs to the cranking regime.

In the present particle-rotor model the M1 operator is written as [10]

$$\begin{aligned}
 M(\text{M1}, \mu) &= \sqrt{\frac{3}{4\pi}} \frac{e\hbar}{2Mc} (g_R R_\mu + g_\ell \ell_\mu + g_s s_\mu) \\
 &= \sqrt{\frac{3}{4\pi}} \frac{e\hbar}{2Mc} (g_R I_\mu + (g_\ell - g_R) \ell_\mu + (g_s - g_R) s_\mu).
 \end{aligned} \tag{9}$$

Since g_R is taken to be a constant, the contributions to M1 transitions come from the second and third terms in (9) and not from the first term $g_R I_\mu$. In the wobbling mode discussed

in the literature [10], in which the intrinsic angular momenta are absent, the meaning of non-zero M1 transitions is very different. First of all, the total angular momentum I is the only vector present in the system. Then, if the M1 operator is proportional to I , namely if the M1 g-factor is just a constant or isotropic, the M1 transitions identically vanish. In order to obtain nonvanishing M1 transitions, the anisotropy of the g-factor must be present.

We compare the ($\Delta I = 1$, E2/M1) transitions in the wobbling regime, from the (α_u , $n_w = 1$) band to the yrast (α_f , $n_w = 0$) band, with those in the case of the α_u band being in the cranking regime. We find that the signature dependence of both B(E2) and B(M1) values in the wobbling regime is out of phase compared with the case of the cranking regime. In the wobbling regime the $\Delta I = 1$ transition is dominated by E2 and not by M1. We summarize the characteristic features of the $\Delta I = 1$ electromagnetic transitions between the α_u wobbling states and the yrast α_f states as follows: (a) B(M1; $\alpha_f I \rightarrow \alpha_u I - 1$) values are reduced, because of $\Delta R_x \approx 2\hbar$; (b) B(E2; $I \rightarrow I - 1$) values are the order of $1/I$ in the limit of high I values, since the wobbling amplitude is the order of $1/\sqrt{I}$; (c) B(E2; $\alpha_f I \rightarrow \alpha_u I - 1$) values are reduced, because the contributions from Q_0 and Q_2 almost cancel for $\gamma = +20^\circ$. On the other hand, the features of those transitions between the α_u states in the cranking regime and the yrast α_f states may be summarized as: (A) both B(M1; $\alpha_u I + 1 \rightarrow \alpha_f I$) and B(E2; $\alpha_u I + 1 \rightarrow \alpha_f I$) values are reduced, because $\Delta R \approx \Delta R_x \approx 2\hbar$ and, simultaneously $\Delta j_x \approx 1\hbar$; (B) B(E2; $I \rightarrow I - 1$) values are small and the order of $1/I^2$ due to the relevant angular momentum algebra [21]; (C) B(M1; $\alpha_f I \rightarrow \alpha_u I - 1$) values are relatively large being of the order of unity.

The $\Delta I = 1$ transitions in the wobbling regime, from the (α_f , $n_w = 2$) band to the (α_u , $n_w = 1$) band, are also dominated by E2 and not by M1. The B(E2; α_f , $n_w = 2$, $I \rightarrow \alpha_u$, $n_w = 1$, $I - 1$) values are of the order of $1/I$ at high I -values, and we expect the relation B(E2; α_f , $n_w = 2$, $I \rightarrow \alpha_u$, $n_w = 1$, $I - 1$) ≈ 2 B(E2; α_u , $n_w = 1$, $I - 1 \rightarrow \alpha_f$, yrast, $I - 2$) due to the boson nature of the wobbling phonon. On the other hand, B(E2; α_f , $n_w = 2$, $I \rightarrow \alpha_f$, yrast, $I - 2$) values are of the order of $1/(I^2)$ and much smaller than the B(E2; α_f , $n_w = 2$, $I \rightarrow \alpha_u$, $n_w = 1$, $I - 1$) values.

6. Comparison to data

In comparison with experimental data for the mixed E2/M1 transitions connecting TSD2 with TSD1, in Fig. 18 we show the calculated B(M1)/B(E2)_{in} and B(E2)_{out}/B(E2)_{in} values of the $\Delta I = 1$ transitions between the wobbling α_{u1} state and the yrast α_{f1} state. We have used the parameters of Fig. 15, which are appropriate for the TSD bands of ^{163}Lu and, consequently, all calculated α_u states are in the wobbling regime. Parameters needed further in the calculation of B(M1) are $g_s^{\text{eff}} = (0.6)g_s^{\text{free}}$ and $g_R = 0.4$. For reference, in the figure we also denote B(M1) and B(E2) values in the “cranking” regime, which are calculated using $\lambda/\kappa = -1.20$ with the parameters of Fig. 17.

The agreement of the present experimental data with the results calculated for the wobbling mode appears quite satisfactory from Fig. 18 and Table 2, in view of the schematic character of the particle-rotor calculations including a single proton $i_{13/2}$ subshell. The

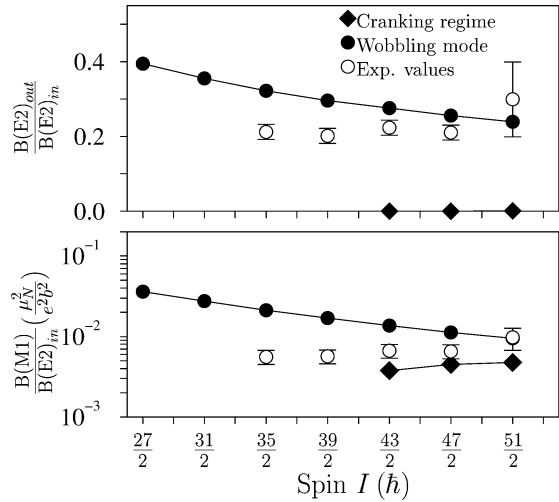


Fig. 18. Experimental and calculated electromagnetic properties of the $\Delta I = 1$, E2/M1 transitions connecting TSD2 to TSD1. Values for the wobbling mode correspond to $n_w = 1 \rightarrow n_w = 0$ transitions.

Table 2

Experimental and calculated values of mixing ratio δ , (average for $35/2\hbar \leq I \leq 51/2\hbar$) branching ratio λ and electromagnetic nature of the connecting transition for $I = 43/2\hbar \rightarrow I = 41/2\hbar$. The theoretical values are based on calculated matrix elements and experimental γ -ray energies. For $I = 43/2\hbar \rightarrow I = 41/2\hbar$ in the cranking regime both E2 and M1 transitions are approximately forbidden. Thus, the sign of the mixing ratio can be either plus or minus

	δ	λ	E/M
exp	$-3.10^{+0.36}_{-0.44}$	0.36 ± 0.04	E
wobbling	-2.4	0.48	E
cranking-like	± 0.15	0.02	M

failure of a cranking-like solution is particularly obvious from the E2 strength, and the extracted properties summarized in Table 2.

The observed gradual increase of B(M1) values is not obtained in the present simple model. It may come from the gradual increase of neutron alignment in the core, which is seen in the observed alignment but not included in the calculation of B(M1) values. With the suggested interpretation of TSD2 as a 1-phonon wobblers, the ratio $\hbar\omega_{\text{wob}}/\hbar\omega_{\text{rot}}$ varies from 1.5 to 0.5 with increasing spin, indicating a gradual change in the three moments of inertia.

The possibility of assigning the higher excited and more weakly populated band, TSD3, as a second phonon wobbling excitation ($n_w = 2$) is also investigated, by comparing the observed relative transition strength from TSD3 to calculations. In Fig. 19 we show the calculated $B(E2; I \rightarrow I - 2)/B(E2)_{\text{in}}$ values of the transitions from the α_{f2} band to the

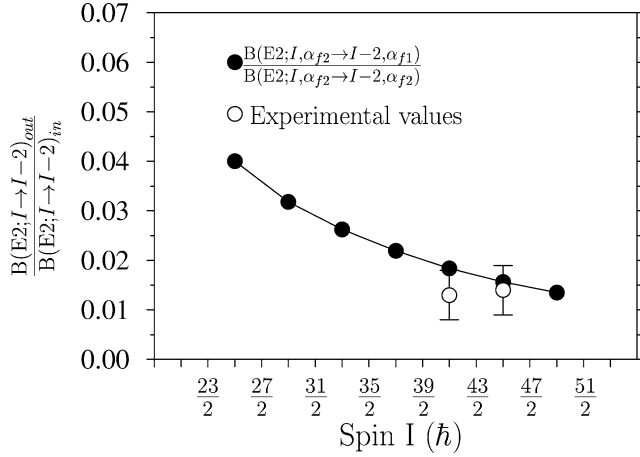


Fig. 19. Calculated $B(E2; I, \alpha_{f2} \rightarrow I-2, \alpha_{f1})/B(E2; I, \alpha_{f2} \rightarrow I-2, \alpha_{f2})$ values for the wobbling mode ($n_w = 2 \rightarrow n_w = 0$), in comparison with the available experimental data on the E2, $I \rightarrow I-2$ transitions from TSD3 to TSD1. Used parameters are the same as those in Fig. 15.

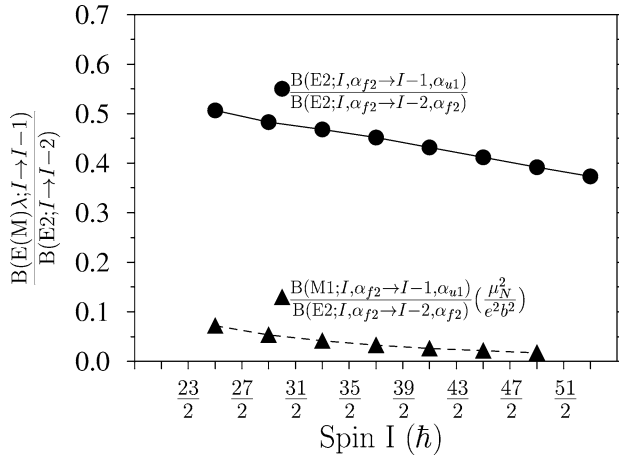


Fig. 20. Calculated $B(E2; I, \alpha_{f2} \rightarrow I-1, \alpha_{u1})/B(E2; I, \alpha_{f2} \rightarrow I-2, \alpha_{f2})$ values and $B(M1; I, \alpha_{f2} \rightarrow I-1, \alpha_{u1})/B(E2; I, \alpha_{f2} \rightarrow I-2, \alpha_{f2})$ values in units of $\mu_N^2 e^{-2} b^{-2}$. ($n_w = 2 \rightarrow n_w = 1$). Used parameters are the same as those in Fig. 15. $g_s^{\text{eff}} = (0.6)g_s^{\text{free}}$ and $g_R = 0.4$. The presently available experimental upper limit of $B(E2; \text{TSD3}, I \rightarrow \text{TSD2}, I-1)/B(E2; \text{TSD3}, I \rightarrow \text{TSD3}, I-2)$ values is 0.67 at $I = 45/2\hbar$.

yrast α_{f1} band ($n_w = 2 \rightarrow n_w = 0$) in comparison with presently available experimental information, while in Fig. 20 the $B(M1; I \rightarrow I-1)/B(E2)_{\text{in}}$ and $B(E2; I \rightarrow I-1)/B(E2)_{\text{in}}$ values of the transitions from the α_{f2} band to the α_{u1} band ($n_w = 2 \rightarrow n_w = 1$) are plotted. The parameters used in the calculation are the same as those used in Fig. 15. The calculated $B(E2; \alpha_{f2}, I \rightarrow \alpha_{f1}, I-2)/B(E2)_{\text{in}}$ values ($\Delta n_w = 2$) in Fig. 19 are in fair agreement with available data on the (E2, $I \rightarrow I-2$) transitions from TSD3 to TSD1. On the other hand, the $B(E2; \alpha_{f2}, I \rightarrow \alpha_{u1}, I-1)/B(E2)_{\text{in}}$ values ($\Delta n_w = 1$) in Fig. 20

are consistent with available experimental information on the TSD3→TSD2 E2 transition strengths, namely they lie below the experimental upper limit. Unlike expectations for the pure harmonic phonon picture, the excitation energy of TSD3 relative to TSD2 is somewhat lower than the excitation of TSD2 relative to TSD1. This observation is in qualitative agreement with the ratio of the calculated energy distance between the α_{f2} and α_{u1} bands to the one between the α_{u1} and α_{f1} bands. On the other hand, one may expect that at this excitation the wobbling mode will to some degree be mixed into possible 3–5 quasiparticle excitations of equal signature and parity.

The α_u band in the cranking regime, which corresponds to our calculated α_{u2} band, has so far never been observed in ^{163}Lu . This fact indicates that the cost of the intrinsic energy in the cranking regime is considerably larger than the one estimated by using the simple intrinsic Hamiltonian, H_{intr} in (1).

7. Summary

New experimental information is presented which provides evidence for the wobbling mode uniquely related to triaxiality, coexisting with well developed band structures in the normal deformed potential energy minimum for ^{163}Lu in a large spin range. Calculations in which one $i_{13/2}$ quasiproton is coupled to a triaxial rotor are presented and the results, in particular concerning the electromagnetic properties, are discussed in comparison with the data.

The candidate for a wobbling excitation in ^{163}Lu , TSD2, has been connected to TSD1 by 9 linking transitions. The electromagnetic properties together with the alignments are in agreement with the assignment of TSD2 as a wobbling excitation in the presence of an aligned particle, built on TSD1. Alternative interpretations as a signature partner or a three-quasiparticle excitation could be rejected. For the first time, the wobbling mode which uniquely proves nuclear triaxiality in the TSD states is established experimentally.

The TSD3 band seems to be a likely candidate of the two-phonon ($n_w = 2$) wobbling mode built on the yrast TSD1 band, since measured alignments as well as moments of inertia of the TSD3 band are very similar to those of the TSD2 and TSD1 bands and since the observed spin-parity is consistent with the $n_w = 2$ assignment. Furthermore, the measured $B(E2; \text{TSD3}, I \rightarrow \text{TSD1}, I - 2)/B(E2)_{\text{in}}$ values are in fair agreement with the calculated $B(E2; \alpha_{f2}, I \rightarrow \alpha_{f1}, I - 2)/B(E2)_{\text{in}}$ values. It is of vital importance to obtain experimentally the $B(E2; \text{TSD3}, I \rightarrow \text{TSD2}, I - 1)$ values, which are expected to be relatively large, in order to pin down the $n_w = 2$ nature of the TSD3 band.

Acknowledgements

This research is supported by the EU TMR project No. ERBFMGECT980145, the EU TMR network project, contract No. ERBFMRXCT970123, the Danish Science Foundation, the Research Council of Norway, the German BMBF (contract No. 06 BN 907) and the Polish State Committee for Scientific Research (KBN Grant No. 2 P03B 045 16).

Appendix

Table A1

ND bands. Level energies, initial and final spin, transition energies, relative intensities (normalised to 1000 for the 630.1 keV transition in the $[523]7/2^-$ band), branching ratios and $B(M1)/B(E2)$ values, extracted from branching ratios, assuming pure $M1 \Delta I = 1$ transitions

Level energy (keV)	$I_i^\pi \rightarrow I_f^\pi$	Transition energy (keV)	Intensity	Branching ratio	$B(M1)/B(E2)$
Band $[411]1/2^+$					
191.0	$\frac{5}{2}^+ \rightarrow \frac{1}{2}^+$	190.9	182(12)		
	$\frac{5}{2}^+ \rightarrow \frac{3}{2}^+$	173.9	77(18)	0.42(10)	0.02(1)
250.0	$\frac{7}{2}^+ \rightarrow \frac{3}{2}^+$	232.9	87(22)		
	$\frac{7}{2}^+ \rightarrow \frac{5}{2}^+$	188.2	50(9)		
520.9	$\frac{9}{2}^+ \rightarrow \frac{5}{2}^+$	329.8	187(26)		
	$\frac{9}{2}^+ \rightarrow \frac{7}{2}^+$	270.9	129(20)	0.67(14)	0.09(2)
620.9	$\frac{11}{2}^+ \rightarrow \frac{7}{2}^+$	370.9	250(35)		
	$\frac{11}{2}^+ \rightarrow \frac{9}{2}^+$	207.0	11(8)		
967.9	$\frac{13}{2}^+ \rightarrow \frac{9}{2}^+$	446.9	229(25)		
	$\frac{13}{2}^+ \rightarrow \frac{11}{2}^+$	347.1	74(15)	0.32(7)	0.10(2)
1106.9	$\frac{15}{2}^+ \rightarrow \frac{11}{2}^+$	486.0	158(20)		
1501.8	$\frac{17}{2}^+ \rightarrow \frac{13}{2}^+$	533.8	139(18)		
	$\frac{17}{2}^+ \rightarrow \frac{15}{2}^+$	394.9	75(11)	0.54(11)	0.14(3)
1669.8	$\frac{19}{2}^+ \rightarrow \frac{15}{2}^+$	563.0	164(22)		
2087.6	$\frac{21}{2}^+ \rightarrow \frac{17}{2}^+$	585.9	183(21)		
2276.7	$\frac{23}{2}^+ \rightarrow \frac{19}{2}^+$	606.9	97(14)		
2773.4	$\frac{27}{2}^+ \rightarrow \frac{23}{2}^+$	496.7	34(8)		
3130.5	$\frac{31}{2}^+ \rightarrow \frac{27}{2}^+$	357.1	27(6)		
3571.7	$\frac{35}{2}^+ \rightarrow \frac{31}{2}^+$	441.3	28(5)		
	$\frac{35}{2}^+ \rightarrow \frac{31}{2}^+$	493.7	49(7)		
	$\frac{35}{2}^+ \rightarrow \frac{33}{2}^+$	248.2	18(4)		
4150.4	$\frac{39}{2}^+ \rightarrow \frac{35}{2}^+$	578.7	182(23)		

Table A1 —continued

Level energy (keV)	$I_i^\pi \rightarrow I_f^\pi$	Transition energy (keV)	Intensity	Branching ratio	B(M1)/B(E2)
4817.0	$\frac{43}{2}^+ \rightarrow \frac{39}{2}^+$	666.5	119(14)		
5559.2	$\frac{47}{2}^+ \rightarrow \frac{43}{2}^+$	742.2	47(9)		
	$\frac{47}{2}^+ \rightarrow \frac{43}{2}^+$	655.2	8(5)		
6355.5	$\frac{51}{2}^+ \rightarrow \frac{47}{2}^+$	796.4	47(9)		
7178.7	$\frac{55}{2}^+ \rightarrow \frac{51}{2}^+$	823.2	13(6)		
8045.8	$\frac{59}{2}^+ \rightarrow \frac{55}{2}^+$	867.1	4(3)		
Band [404]7/2 ⁺					
123.9	$\frac{7}{2}^+ \rightarrow \frac{5}{2}^+$	62.1	56(20)		
310.1	$\frac{9}{2}^+ \rightarrow \frac{7}{2}^+$	186.2	184(26)		
520.1	$\frac{11}{2}^+ \rightarrow \frac{7}{2}^+$	396.5	297(28)		
	$\frac{11}{2}^+ \rightarrow \frac{9}{2}^+$	210.3	172(17)	0.58(8)	0.43(6)
	$\frac{11}{2}^+ \rightarrow \frac{9}{2}^+$	106.2	49(5)		
754.4	$\frac{13}{2}^+ \rightarrow \frac{9}{2}^+$	444.3	438(34)		
	$\frac{13}{2}^+ \rightarrow \frac{11}{2}^+$	234.3	165(15)	0.38(5)	0.36(4)
1007.8	$\frac{15}{2}^+ \rightarrow \frac{11}{2}^+$	487.7	632(48)		
	$\frac{15}{2}^+ \rightarrow \frac{13}{2}^+$	253.4	169(14)	0.27(3)	0.32(4)
1282.1	$\frac{17}{2}^+ \rightarrow \frac{13}{2}^+$	527.8	399(36)		
	$\frac{17}{2}^+ \rightarrow \frac{15}{2}^+$	274.3	97(10)	0.24(3)	0.34(5)
1561.7	$\frac{19}{2}^+ \rightarrow \frac{15}{2}^+$	553.9	731(52)		
	$\frac{19}{2}^+ \rightarrow \frac{17}{2}^+$	279.6	189(16)	0.26(3)	0.43(5)
1867.3	$\frac{21}{2}^+ \rightarrow \frac{17}{2}^+$	585.2	353(29)		
	$\frac{21}{2}^+ \rightarrow \frac{19}{2}^+$	305.6	91(13)	0.26(4)	0.43(7)
2139.3	$\frac{23}{2}^+ \rightarrow \frac{19}{2}^+$	577.7	611(45)		
	$\frac{23}{2}^+ \rightarrow \frac{21}{2}^+$	272.0	93(11)	0.15(2)	0.34(5)
	$\frac{23}{2}^+ \rightarrow \frac{21}{2}^-$	653.8	93(12)		

Table A1—continued

Level energy (keV)	$I_i^\pi \rightarrow I_f^\pi$	Transition energy (keV)	Intensity	Branching ratio	B(M1)/B(E2)
2400.2	$\frac{25}{2}^+ \rightarrow \frac{21}{2}^+$	532.8	127(12)		
	$\frac{25}{2}^+ \rightarrow \frac{23}{2}^+$	260.8	239(19)	1.88(23)	3.17(39)
	$\frac{25}{2}^+ \rightarrow \frac{21}{2}^+$	391.5	29(6)		
	$\frac{25}{2}^+ \rightarrow \frac{21}{2}^+$	379.9	73(8)		
	$\frac{25}{2}^+ \rightarrow \frac{23}{2}^-$	723.1	137(13)		
	$\frac{25}{2}^+ \rightarrow \frac{23}{2}^+$	172.2	49(6)		
2614.2	$\frac{27}{2}^+ \rightarrow \frac{23}{2}^+$	474.7	169(14)		
	$\frac{27}{2}^+ \rightarrow \frac{25}{2}^+$	214.0	294(28)	1.74(22)	2.98(38)
	$\frac{27}{2}^+ \rightarrow \frac{23}{2}^+$	386.2	34(5)		
	$\frac{27}{2}^+ \rightarrow \frac{25}{2}^-$	510.1	79(8)		
2803.1	$\frac{29}{2}^+ \rightarrow \frac{25}{2}^+$	403.2	131(12)		
	$\frac{29}{2}^+ \rightarrow \frac{27}{2}^+$	189.0	186(26)	1.42(26)	1.56(26)
	$\frac{29}{2}^+ \rightarrow \frac{25}{2}^+$	313.9	17(4)		
	$\frac{29}{2}^+ \rightarrow \frac{27}{2}^+$	117.9	7(3)		
3003.6	$\frac{31}{2}^+ \rightarrow \frac{27}{2}^+$	389.7	144(14)		
	$\frac{31}{2}^+ \rightarrow \frac{29}{2}^+$	200.4	314(33)	2.18(31)	1.70(24)
	$\frac{31}{2}^+ \rightarrow \frac{27}{2}^+$	318.4	< 5		
3244.7	$\frac{33}{2}^+ \rightarrow \frac{29}{2}^+$	441.5	270(21)		
	$\frac{33}{2}^+ \rightarrow \frac{31}{2}^+$	241.2	268(21)	0.99(11)	0.83(9)
3483.3	$\frac{35}{2}^+ \rightarrow \frac{31}{2}^+$	479.7	262(22)		
	$\frac{35}{2}^+ \rightarrow \frac{33}{2}^+$	238.6	184(15)	0.70(8)	0.91(11)
3789.3	$\frac{37}{2}^+ \rightarrow \frac{33}{2}^+$	544.7	235(18)		
	$\frac{37}{2}^+ \rightarrow \frac{35}{2}^+$	306.1	271(21)	1.15(13)	1.34(15)
4067.7	$\frac{39}{2}^+ \rightarrow \frac{35}{2}^+$	584.5	359(27)		
	$\frac{39}{2}^+ \rightarrow \frac{37}{2}^+$	278.4	230(17)	0.64(7)	1.41(15)

Table A1 —continued

Level energy (keV)	$I_i^\pi \rightarrow I_f^\pi$	Transition energy (keV)	Intensity	Branching ratio	B(M1)/B(E2)
4405.4	$\frac{41}{2}^+ \rightarrow \frac{37}{2}^+$	616.2	277(22)		
	$\frac{41}{2}^+ \rightarrow \frac{39}{2}^+$	337.7	161(38)	0.58(14)	0.94(23)
4719.1	$\frac{43}{2}^+ \rightarrow \frac{39}{2}^+$	651.3	456(34)		
	$\frac{43}{2}^+ \rightarrow \frac{41}{2}^+$	313.7	159(12)	0.35(4)	0.92(10)
5056.9	$\frac{45}{2}^+ \rightarrow \frac{41}{2}^+$	652.6	314(24)		
	$\frac{45}{2}^+ \rightarrow \frac{43}{2}^+$	337.8	189(40)	0.60(14)	1.28(29)
5387.3	$\frac{47}{2}^+ \rightarrow \frac{43}{2}^+$	668.0	225(22)		
	$\frac{47}{2}^+ \rightarrow \frac{45}{2}^+$	330.4	143(15)	0.64(9)	1.62(23)
5719.4	$\frac{49}{2}^+ \rightarrow \frac{45}{2}^+$	662.8	175(20)		
	$\frac{49}{2}^+ \rightarrow \frac{47}{2}^+$	332.1	99(10)	0.57(9)	1.38(21)
6064.8	$\frac{51}{2}^+ \rightarrow \frac{47}{2}^+$	677.1	147(15)		
	$\frac{51}{2}^+ \rightarrow \frac{49}{2}^+$	345.4	91(10)	0.62(9)	1.48(22)
6414.5	$\frac{53}{2}^+ \rightarrow \frac{49}{2}^+$	695.0	164(17)		
	$\frac{53}{2}^+ \rightarrow \frac{51}{2}^+$	349.6	106(10)	0.65(9)	1.71(24)
6788.2	$\frac{55}{2}^+ \rightarrow \frac{51}{2}^+$	723.7	140(14)		
	$\frac{55}{2}^+ \rightarrow \frac{53}{2}^+$	373.7	60(6)	0.43(6)	1.14(16)
7173.7	$\frac{57}{2}^+ \rightarrow \frac{53}{2}^+$	758.8	100(11)		
	$\frac{57}{2}^+ \rightarrow \frac{55}{2}^+$	385.5	49(10)	0.49(11)	1.50(35)
7584.0	$\frac{59}{2}^+ \rightarrow \frac{55}{2}^+$	795.5	89(9)		
	$\frac{59}{2}^+ \rightarrow \frac{57}{2}^+$	410.2	45(4)	0.51(7)	1.62(21)
8010.4	$\frac{61}{2}^+ \rightarrow \frac{57}{2}^+$	837.5	73(7)		
	$\frac{61}{2}^+ \rightarrow \frac{59}{2}^+$	426.4	35(4)	0.48(7)	1.78(26)
8458.3	$\frac{63}{2}^+ \rightarrow \frac{59}{2}^+$	875.5	45(5)		
	$\frac{63}{2}^+ \rightarrow \frac{61}{2}^+$	447.9	23(6)	0.51(15)	2.04(58)
8924.5	$\frac{65}{2}^+ \rightarrow \frac{61}{2}^+$	915.6	45(11)		
9406.2	$\frac{67}{2}^+ \rightarrow \frac{63}{2}^+$	949.3	25(6)		
9912.7	$\frac{69}{2}^+ \rightarrow \frac{65}{2}^+$	989.2	21(7)		

Table A1 —continued

Level energy (keV)	$I_i^\pi \rightarrow I_f^\pi$	Transition energy (keV)	Intensity	Branching ratio	B(M1)/B(E2)
10422.1	$\frac{71}{2}^+ \rightarrow \frac{67}{2}^+$	1015.9	21(7)		
10974.4	$\frac{73}{2}^+ \rightarrow \frac{69}{2}^+$	1061.6	10(3)		
11500.2	$\frac{75}{2}^+ \rightarrow \frac{71}{2}^+$	1078.1	3(2)		
12094.0	$\frac{77}{2}^+ \rightarrow \frac{73}{2}^+$	1119.7	12(3)		
12622.0	$\frac{79}{2}^+ \rightarrow \frac{75}{2}^+$	1121.8	2(2)		
Band [402]5/2 ⁺					
61.8	$\frac{5}{2}^+$				
224.0	$\frac{7}{2}^+ \rightarrow \frac{5}{2}^+$	162.2	102(22)		
413.9	$\frac{9}{2}^+ \rightarrow \frac{5}{2}^+$	352.0	46(12)		
	$\frac{9}{2}^+ \rightarrow \frac{7}{2}^+$	189.8	88(31)	1.91(15)	1.07(9)
641.9	$\frac{11}{2}^+ \rightarrow \frac{7}{2}^+$	417.8	106(14)		
	$\frac{11}{2}^+ \rightarrow \frac{9}{2}^+$	228.0	71(17)	0.67(18)	0.50(14)
874.9	$\frac{13}{2}^+ \rightarrow \frac{9}{2}^+$	461.0	88(18)		
	$\frac{13}{2}^+ \rightarrow \frac{11}{2}^+$	233.0	80(13)	0.91(21)	1.04(24)
1152.1	$\frac{15}{2}^+ \rightarrow \frac{11}{2}^+$	510.2	71(12)		
	$\frac{15}{2}^+ \rightarrow \frac{13}{2}^+$	277.2	65(12)	0.92(34)	1.03(38)
1416.7	$\frac{17}{2}^+ \rightarrow \frac{13}{2}^+$	541.8	92(14)		
	$\frac{17}{2}^+ \rightarrow \frac{15}{2}^+$	264.6	25(9)	0.27(11)	0.48(19)
1729.8	$\frac{19}{2}^+ \rightarrow \frac{15}{2}^+$	577.7	27(15)		
	$\frac{19}{2}^+ \rightarrow \frac{17}{2}^+$	313.1	12(9)	0.44(42)	0.66(62)
2020.2	$\frac{21}{2}^+ \rightarrow \frac{17}{2}^+$	603.5	60(10)		
	$\frac{21}{2}^+ \rightarrow \frac{19}{2}^+$	(290.5)	< 5		
2339.3	$\frac{23}{2}^+ \rightarrow \frac{19}{2}^+$	609.6	8(8)		
	$\frac{23}{2}^+ \rightarrow \frac{21}{2}^+$	(319.1)	< 5		

Table A1—continued

Level energy (keV)	$I_i^\pi \rightarrow I_f^\pi$	Transition energy (keV)	Intensity	Branching ratio	B(M1)/B(E2)
Band [523]7/2 ⁻					
194.6	$\frac{7}{2}^- \rightarrow \frac{5}{2}^+$	132.8	65(22)		
	$\frac{7}{2}^- \rightarrow \frac{7}{2}^+$	70.7	43(30)		
209.8	$\frac{9}{2}^- \rightarrow \frac{7}{2}^+$	85.9	135(27)		
295.2	$\frac{11}{2}^- \rightarrow \frac{9}{2}^-$	85.4	55(12)		
491.8	$\frac{13}{2}^- \rightarrow \frac{9}{2}^-$	282.0	191(22)		
	$\frac{13}{2}^- \rightarrow \frac{11}{2}^-$	196.6	490(38)	2.57(36)	0.42(6)
644.4	$\frac{15}{2}^- \rightarrow \frac{11}{2}^-$	349.2	717(37)		
	$\frac{15}{2}^- \rightarrow \frac{13}{2}^-$	152.7	400(29)	0.56(5)	0.57(5)
937.1	$\frac{17}{2}^- \rightarrow \frac{13}{2}^-$	445.3	374(21)		
	$\frac{17}{2}^- \rightarrow \frac{15}{2}^-$	292.6	452(34)	1.21(11)	0.59(6)
1115.0	$\frac{19}{2}^- \rightarrow \frac{15}{2}^-$	470.6	792(56)		
	$\frac{19}{2}^- \rightarrow \frac{17}{2}^-$	178.0	190(22)	0.24(3)	0.68(8)
1485.5	$\frac{21}{2}^- \rightarrow \frac{17}{2}^-$	548.5	295(22)		
	$\frac{21}{2}^- \rightarrow \frac{19}{2}^-$	370.5	248(24)	0.84(10)	0.57(7)
1677.1	$\frac{23}{2}^- \rightarrow \frac{19}{2}^-$	562.0	1174(81)		
	$\frac{23}{2}^- \rightarrow \frac{21}{2}^-$	191.5	160(14)	0.14(2)	0.76(8)
2104.0	$\frac{25}{2}^- \rightarrow \frac{21}{2}^-$	618.7	387(31)		
	$\frac{25}{2}^- \rightarrow \frac{23}{2}^-$	427.0	378(26)	0.98(10)	0.79(8)
2307.3	$\frac{27}{2}^- \rightarrow \frac{23}{2}^-$	630.1	1000(50)		
	$\frac{27}{2}^- \rightarrow \frac{25}{2}^-$	203.2	137(20)	0.14(2)	1.13(17)
2747.9	$\frac{29}{2}^- \rightarrow \frac{25}{2}^-$	643.8	210(18)		
	$\frac{29}{2}^- \rightarrow \frac{27}{2}^-$	440.6	144(15)	0.69(9)	0.62(8)
2924.7	$\frac{31}{2}^- \rightarrow \frac{27}{2}^-$	617.5	864(60)		
	$\frac{31}{2}^- \rightarrow \frac{29}{2}^-$	176.9	121(14)	0.14(2)	1.58(21)

Table A1—continued

Level energy (keV)	$I_i^\pi \rightarrow I_f^\pi$	Transition energy (keV)	Intensity	Branching ratio	B(M1)/B(E2)
3123.3	$\frac{33}{2}^- \rightarrow \frac{29}{2}^-$	374.7	80(10)		
	$\frac{33}{2}^- \rightarrow \frac{31}{2}^-$	198.6	396(48)	4.95(86)	3.25(57)
	$\frac{33}{2}^- \rightarrow \frac{31}{2}^-$	102.0	25(3)		
	$\frac{33}{2}^- \rightarrow \frac{29}{2}^-$	268.1	40(11)		
3320.6	$\frac{35}{2}^- \rightarrow \frac{31}{2}^-$	396.0	95(15)		
	$\frac{35}{2}^- \rightarrow \frac{33}{2}^-$	197.3	475(83)	5.0(12)	4.4(10)
	$\frac{35}{2}^- \rightarrow \frac{31}{2}^-$	299.3	< 5		
3551.6	$\frac{37}{2}^- \rightarrow \frac{33}{2}^-$	428.4	242(19)		
	$\frac{37}{2}^- \rightarrow \frac{35}{2}^-$	231.0	868(59)	3.59(37)	2.92(30)
3822.5	$\frac{39}{2}^- \rightarrow \frac{35}{2}^-$	501.9	260(19)		
	$\frac{39}{2}^- \rightarrow \frac{37}{2}^-$	270.9	634(44)	2.44(25)	2.72(27)
4103.7	$\frac{41}{2}^- \rightarrow \frac{37}{2}^-$	552.1	338(25)		
	$\frac{41}{2}^- \rightarrow \frac{39}{2}^-$	281.2	570(40)	1.69(17)	2.71(28)
4431.3	$\frac{43}{2}^- \rightarrow \frac{39}{2}^-$	608.8	238(19)		
	$\frac{43}{2}^- \rightarrow \frac{41}{2}^-$	327.6	240(24)	1.01(13)	1.67(21)
4760.5	$\frac{45}{2}^- \rightarrow \frac{41}{2}^-$	656.6	222(18)		
	$\frac{45}{2}^- \rightarrow \frac{43}{2}^-$	329.2	133(20)	0.60(10)	1.43(24)
5131.4	$\frac{47}{2}^- \rightarrow \frac{43}{2}^-$	700.7	153(14)		
	$\frac{47}{2}^- \rightarrow \frac{45}{2}^-$	371.0	172(21)	1.12(17)	2.59(40)
5504.8	$\frac{49}{2}^- \rightarrow \frac{45}{2}^-$	744.3	187(15)		
	$\frac{49}{2}^- \rightarrow \frac{47}{2}^-$	373.4	160(14)	0.86(10)	2.61(31)
5916.3	$\frac{51}{2}^- \rightarrow \frac{47}{2}^-$	785.2	93(10)		
	$\frac{51}{2}^- \rightarrow \frac{49}{2}^-$	411.5	85(9)	0.91(14)	2.73(41)
6333.5	$\frac{53}{2}^- \rightarrow \frac{49}{2}^-$	829.0	104(10)		
	$\frac{53}{2}^- \rightarrow \frac{51}{2}^-$	417.2	67(8)	0.64(10)	2.42(37)

Table A1 —continued

Level energy (keV)	$I_i^\pi \rightarrow I_f^\pi$	Transition energy (keV)	Intensity	Branching ratio	B(M1)/B(E2)
6789.5	$\frac{55}{2}^- \rightarrow \frac{51}{2}^-$	872.7	85(9)		
	$\frac{55}{2}^- \rightarrow \frac{53}{2}^-$	456.0	85(9)	1.00(15)	3.72(56)
7246.4	$\frac{57}{2}^- \rightarrow \frac{53}{2}^-$	913.0	73(8)		
	$\frac{57}{2}^- \rightarrow \frac{55}{2}^-$	456.8	12(6)		
7728.8	$\frac{59}{2}^- \rightarrow \frac{55}{2}^-$	939.2	35(10)		
	$\frac{59}{2}^- \rightarrow \frac{57}{2}^-$	482.4	< 5		
8222.3	$\frac{61}{2}^- \rightarrow \frac{57}{2}^-$	975.9	25(13)		
8713.1	$\frac{63}{2}^- \rightarrow \frac{59}{2}^-$	984.3	14(6)		
9252.3	$\frac{65}{2}^- \rightarrow \frac{61}{2}^-$	1030.0	7(4)		
9708.5	$\frac{67}{2}^- \rightarrow \frac{63}{2}^-$	995.4	10(5)		
10264.5	$\frac{69}{2}^- \rightarrow \frac{65}{2}^-$	1012.3	< 5		
10714.4	$\frac{71}{2}^- \rightarrow \frac{67}{2}^-$	1005.9	< 5		
Band X1					
4309.1	$(\frac{39}{2}^-) \rightarrow \frac{35}{2}^-$	988.6	< 5		
	$(\frac{39}{2}^-) \rightarrow \frac{37}{2}^-$	757.6	56(14)		
4578.8	$(\frac{41}{2}^-) \rightarrow \frac{37}{2}^-$	1027.1	7(3)		
	$(\frac{41}{2}^-) \rightarrow \frac{39}{2}^-$	756.4	39(9)		
	$(\frac{41}{2}^-) \rightarrow (\frac{39}{2}^-)$	269.7	43(10)		
4831.0	$(\frac{43}{2}^-) \rightarrow (\frac{39}{2}^-)$	522.0	38(9)		
	$(\frac{43}{2}^-) \rightarrow (\frac{41}{2}^-)$	252.2	52(13)	1.38(49)	2.31(80)
	$(\frac{43}{2}^-) \rightarrow \frac{41}{2}^-$	727.3	25(5)		
5115.9	$(\frac{45}{2}^-) \rightarrow (\frac{41}{2}^-)$	537.3	21(5)		
	$(\frac{45}{2}^-) \rightarrow (\frac{43}{2}^-)$	285.1	23(6)	1.08(38)	1.45(50)
	$(\frac{45}{2}^-) \rightarrow \frac{41}{2}^-$	1012.2	7(3)		
	$(\frac{45}{2}^-) \rightarrow \frac{43}{2}^-$	684.3	< 5		

Table A1 —continued

Level energy (keV)	$I_i^\pi \rightarrow I_f^\pi$	Transition energy (keV)	Intensity	Branching ratio	B(M1)/B(E2)
5419.3	$(\frac{47}{2}^-) \rightarrow (\frac{43}{2}^-)$	588.4	32(8)		
	$(\frac{47}{2}^-) \rightarrow (\frac{45}{2}^-)$	303.3	27(7)	0.85(30)	1.49(52)
5756.8	$(\frac{49}{2}^-) \rightarrow (\frac{45}{2}^-)$	640.7	34(9)		
	$(\frac{49}{2}^-) \rightarrow (\frac{47}{2}^-)$	337.4	25(6)	0.73(26)	1.43(50)
	$(\frac{49}{2}^-) \rightarrow \frac{45}{2}^-$	(996.4)	< 5		
6108.0	$(\frac{51}{2}^-) \rightarrow (\frac{47}{2}^-)$	688.7	48(12)		
	$(\frac{51}{2}^-) \rightarrow (\frac{49}{2}^-)$	351.2	24(6)	0.50(17)	1.24(43)
6502.5	$(\frac{53}{2}^-) \rightarrow (\frac{49}{2}^-)$	745.7	66(17)		
	$(\frac{53}{2}^-) \rightarrow (\frac{51}{2}^-)$	394.5	34(9)	0.52(18)	1.36(47)
6907.2	$(\frac{55}{2}^-) \rightarrow (\frac{51}{2}^-)$	799.2	26(6)		
	$(\frac{55}{2}^-) \rightarrow (\frac{53}{2}^-)$	404.7	11(3)	0.41(14)	1.41(49)
7351.0	$(\frac{57}{2}^-) \rightarrow (\frac{53}{2}^-)$	848.5	19(5)		
7813.7	$(\frac{59}{2}^-) \rightarrow (\frac{55}{2}^-)$	906.5	17(4)		
8291.2	$(\frac{61}{2}^-) \rightarrow (\frac{57}{2}^-)$	940.0	13(3)		
8790.1	$(\frac{63}{2}^-) \rightarrow (\frac{59}{2}^-)$	976.4	9(3)		
9284.4	$(\frac{65}{2}^-) \rightarrow (\frac{61}{2}^-)$	993.4	5(4)		
10346.4	$(\frac{69}{2}^-) \rightarrow (\frac{65}{2}^-)$	(1062.0)	5(5)		
Band X2					
2410.5	$\frac{21}{2}^+ \rightarrow \frac{19}{2}^+$	680.7	14(11)		
2436.7	$\frac{23}{2}^+ \rightarrow \frac{19}{2}^+$	706.9	8(7)		
	$\frac{23}{2}^+ \rightarrow \frac{21}{2}^-$	951.2	5(5)		
2540.5	$\frac{25}{2}^+ \rightarrow \frac{21}{2}^+$	130.0	9(2)		
	$\frac{25}{2}^+ \rightarrow \frac{23}{2}^+$	103.8	7(1)		
	$\frac{25}{2}^+ \rightarrow \frac{23}{2}^-$	863.4	13(6)		
2680.7	$\frac{27}{2}^+ \rightarrow \frac{23}{2}^+$	244.0	18(3)		
	$\frac{27}{2}^+ \rightarrow \frac{25}{2}^+$	140.3	57(7)	3.17(66)	0.69(14)

Table A1—continued

Level energy (keV)	$I_i^\pi \rightarrow I_f^\pi$	Transition energy (keV)	Intensity	Branching ratio	B(M1)/B(E2)
2860.9	$\frac{29}{2}^+ \rightarrow \frac{25}{2}^+$	320.4	41(9)		
	$\frac{29}{2}^+ \rightarrow \frac{27}{2}^+$	180.2	98(9)	2.39(57)	0.96(23)
3078.1	$\frac{31}{2}^+ \rightarrow \frac{27}{2}^+$	397.3	127(13)		
	$\frac{31}{2}^+ \rightarrow \frac{29}{2}^+$	217.2	136(13)	1.07(15)	0.72(10)
3323.5	$\frac{33}{2}^+ \rightarrow \frac{29}{2}^+$	462.7	31(11)		
	$\frac{33}{2}^+ \rightarrow \frac{31}{2}^+$	245.5	38(9)	1.23(52)	1.22(52)
3892.3	$\frac{37}{2}^+ \rightarrow \frac{33}{2}^+$	568.6	9(3)		
	$\frac{37}{2}^+ \rightarrow \frac{35}{2}^+$	320.4	22(6)	2.4(11)	4.4(19)
4529.3	$\frac{41}{2}^+ \rightarrow \frac{37}{2}^+$	636.8	38(8)		
4904.0	$\frac{43}{2}^+ \rightarrow \frac{41}{2}^+$	374.6	30(9)		
5209.4	$\frac{45}{2}^+ \rightarrow \frac{41}{2}^+$	680.1	17(5)		
	$\frac{45}{2}^+ \rightarrow \frac{43}{2}^+$	305.5	8(6)	0.5(4)	1.7(14)
5557.2	$\frac{47}{2}^+ \rightarrow \frac{43}{2}^+$	653.4	21(5)		
	$\frac{47}{2}^+ \rightarrow \frac{45}{2}^+$	347.9	18(12)	0.9(6)	1.7(12)
	$\frac{47}{2}^+ \rightarrow \frac{43}{2}^+$	740.0	31(5)		
5897.9	$\frac{49}{2}^+ \rightarrow \frac{45}{2}^+$	688.5	16(7)		
	$\frac{49}{2}^+ \rightarrow \frac{47}{2}^+$	340.8	10(6)	0.6(5)	1.7(13)
	$\frac{49}{2}^+ \rightarrow \frac{47}{2}^+$	338.8	12(2)		
6246.2	$\frac{51}{2}^+ \rightarrow \frac{47}{2}^+$	689.1	58(13)		
	$\frac{51}{2}^+ \rightarrow \frac{49}{2}^+$	348.3	45(17)	0.8(3)	2.0(9)
	$\frac{51}{2}^+ \rightarrow \frac{47}{2}^+$	686.8	< 10		
6616.2	$\frac{53}{2}^+ \rightarrow \frac{49}{2}^+$	718.4	15(4)		
	$\frac{53}{2}^+ \rightarrow \frac{51}{2}^+$	370.0	11(6)	0.7(5)	1.9(12)
6979.8	$\frac{55}{2}^+ \rightarrow \frac{51}{2}^+$	733.5	14(3)		
	$\frac{55}{2}^+ \rightarrow \frac{53}{2}^+$	363.6	9(3)	0.64(26)	1.98(78)

Table A1 —continued

Level energy (keV)	$I_i^\pi \rightarrow I_f^\pi$	Transition energy (keV)	Intensity	Branching ratio	B(M1)/B(E2)
7390.7	$\frac{57}{2}^+ \rightarrow \frac{53}{2}^+$	774.5	22(3)		
	$\frac{57}{2}^+ \rightarrow \frac{55}{2}^+$	410.9	15(3)	0.68(17)	1.57(38)
7785.0	$\frac{59}{2}^+ \rightarrow \frac{55}{2}^+$	805.3	30(4)		
	$\frac{59}{2}^+ \rightarrow \frac{57}{2}^+$	394.3	14(4)	0.47(15)	1.79(57)
8237.0	$\frac{61}{2}^+ \rightarrow \frac{57}{2}^+$	846.3	23(3)		
	$\frac{61}{2}^+ \rightarrow \frac{59}{2}^+$	452.0	13(3)	0.57(15)	1.85(49)
8668.4	$\frac{63}{2}^+ \rightarrow \frac{59}{2}^+$	883.4	21(4)		
	$\frac{63}{2}^+ \rightarrow \frac{61}{2}^+$	431.4	12(3)	0.57(18)	2.67(84)
9153.9	$\frac{65}{2}^+ \rightarrow \frac{61}{2}^+$	916.8	14(4)		
	$\frac{65}{2}^+ \rightarrow \frac{63}{2}^+$	485.5	10(4)	0.7(4)	2.8(14)
9625.2	$\frac{67}{2}^+ \rightarrow \frac{63}{2}^+$	956.8	5(3)		
	$\frac{67}{2}^+ \rightarrow \frac{65}{2}^+$	471.3	< 5		
10138.2	$\frac{69}{2}^+ \rightarrow \frac{65}{2}^+$	984.4			
	$\frac{69}{2}^+ \rightarrow \frac{67}{2}^+$	(513.0)			
10653.2	$\frac{71}{2}^+ \rightarrow \frac{67}{2}^+$	1028.0			
	$\frac{71}{2}^+ \rightarrow \frac{69}{2}^+$	(515.0)			
11186.5	$\frac{73}{2}^+ \rightarrow \frac{69}{2}^+$	1048.3			
11748.7	$\frac{75}{2}^+ \rightarrow \frac{71}{2}^+$	1095.5			
Other levels					
2008.7	$\frac{21}{2}^+ \rightarrow \frac{17}{2}^+$	592.0	28(8)		
	$\frac{21}{2}^+ \rightarrow \frac{19}{2}^-$	893.7	12(8)		
2228.0	$\frac{23}{2}^+ \rightarrow \frac{21}{2}^-$	742.5	32(8)		
	$\frac{23}{2}^+ \rightarrow \frac{19}{2}^+$	666.3	40(15)		
2489.2	$\frac{25}{2}^+ \rightarrow \frac{21}{2}^+$	(480.5)	9(8)		
	$\frac{25}{2}^+ \rightarrow \frac{21}{2}^+$	621.9	107(14)		
2685.2	$\frac{27}{2}^+ \rightarrow \frac{25}{2}^-$	581.2	18(10)		
	$\frac{27}{2}^+ \rightarrow \frac{23}{2}^+$	545.9	136(16)		
2855.2	$\frac{29}{2}^- \rightarrow \frac{25}{2}^-$	751.2	61(17)		
3021.3	$\frac{31}{2}^- \rightarrow \frac{27}{2}^-$	714.0	165(13)		

Table A2

TSD bands. Level energies, initial and final spin, transition energies, relative intensities (multiplied by a factor of 7.25 relative to Table A1, corresponding to 1000 for the 386.3 keV transition in TSD1) and branching ratios

Level energy (keV)	$I_i^\pi \rightarrow I_f^\pi$	Transition energy (keV)	Intensity
Band TSD1			
1936.4	$\frac{17}{2}^+ \rightarrow \frac{13}{2}^+$	196.7	89(50)
	$\frac{17}{2}^+ \rightarrow \frac{15}{2}^-$	1292.0	< 5
2199.6	$\frac{21}{2}^+ \rightarrow \frac{17}{2}^+$	263.3	38(20)
	$\frac{21}{2}^+ \rightarrow \frac{17}{2}^+$	697.8	18(10)
	$\frac{21}{2}^+ \rightarrow \frac{19}{2}^+$	529.8	< 5
2514.5	$\frac{25}{2}^+ \rightarrow \frac{21}{2}^+$	314.8	767(100)
	$\frac{25}{2}^+ \rightarrow \frac{21}{2}^+$	505.8	39(20)
	$\frac{25}{2}^+ \rightarrow \frac{21}{2}^+$	426.8	180(30)
2900.8	$\frac{29}{2}^+ \rightarrow \frac{25}{2}^+$	386.3	1000(50)
3351.1	$\frac{33}{2}^+ \rightarrow \frac{29}{2}^+$	450.3	964(86)
3866.4	$\frac{37}{2}^+ \rightarrow \frac{33}{2}^+$	515.3	869(78)
4445.0	$\frac{41}{2}^+ \rightarrow \frac{37}{2}^+$	578.6	792(76)
5084.0	$\frac{45}{2}^+ \rightarrow \frac{41}{2}^+$	639.0	631(57)
5780.9	$\frac{49}{2}^+ \rightarrow \frac{45}{2}^+$	697.0	483(50)
6533.5	$\frac{53}{2}^+ \rightarrow \frac{49}{2}^+$	752.6	373(37)
7339.1	$\frac{57}{2}^+ \rightarrow \frac{53}{2}^+$	805.6	292(31)
8196.8	$\frac{61}{2}^+ \rightarrow \frac{57}{2}^+$	857.7	169(23)
9106.5	$\frac{65}{2}^+ \rightarrow \frac{61}{2}^+$	909.7	135(19)
10069.0	$\frac{69}{2}^+ \rightarrow \frac{65}{2}^+$	962.5	70(12)
11085.5	$\frac{73}{2}^+ \rightarrow \frac{69}{2}^+$	1016.5	50(12)
12156.6	$\frac{77}{2}^+ \rightarrow \frac{73}{2}^+$	1071.1	35(10)
13282.8	$\frac{81}{2}^+ \rightarrow \frac{77}{2}^+$	1126.2	12(5)
14462.1	$\frac{85}{2}^+ \rightarrow \frac{81}{2}^+$	1179.3	11(5)

Table A2—continued

Level energy (keV)	$I_i^\pi \rightarrow I_f^\pi$	Transition energy (keV)	Intensity	Branching ratio
15689.1	$\frac{89}{2}^+ \rightarrow \frac{85}{2}^+$	1227.0	11(5)	
16958.1	$\frac{93}{2}^+ \rightarrow \frac{89}{2}^+$	1269.0	9(5)	
18264.6	$\frac{97}{2}^+ \rightarrow \frac{93}{2}^+$	(1306.5)	7(4)	
Band TSD2				
3079.2	$\frac{27}{2}^+ \rightarrow \frac{25}{2}^+$	564.8	53(20)	
3486.6	$\frac{31}{2}^+ \rightarrow \frac{27}{2}^+$	407.4	50(19)	
	$\frac{31}{2}^+ \rightarrow \frac{29}{2}^+$	585.9	72(25)	1.44(74)
3958.2	$\frac{35}{2}^+ \rightarrow \frac{31}{2}^+$	471.6	106(7)	
	$\frac{35}{2}^+ \rightarrow \frac{33}{2}^+$	607.1	88(6)	0.83(8)
4492.5	$\frac{39}{2}^+ \rightarrow \frac{35}{2}^+$	534.3	115(8)	
	$\frac{39}{2}^+ \rightarrow \frac{37}{2}^+$	626.2	56(4)	0.49(5)
5088.3	$\frac{43}{2}^+ \rightarrow \frac{39}{2}^+$	595.8	120(8)	
	$\frac{43}{2}^+ \rightarrow \frac{41}{2}^+$	643.3	43(3)	0.36(4)
5742.9	$\frac{47}{2}^+ \rightarrow \frac{43}{2}^+$	654.6	140(9)	
	$\frac{47}{2}^+ \rightarrow \frac{45}{2}^+$	658.9	34(3)	0.24(3)
6454.1	$\frac{51}{2}^+ \rightarrow \frac{47}{2}^+$	711.2	134(20)	
	$\frac{51}{2}^+ \rightarrow \frac{49}{2}^+$	673.2	34(10)	0.25(9)
7220.3	$\frac{55}{2}^+ \rightarrow \frac{51}{2}^+$	766.2	111(20)	
	$\frac{55}{2}^+ \rightarrow \frac{53}{2}^+$	686.8	17(5)	0.15(5)
8040.2	$\frac{59}{2}^+ \rightarrow \frac{55}{2}^+$	819.9	90(14)	
	$\frac{59}{2}^+ \rightarrow \frac{57}{2}^+$	701.1	11(4)	0.12(5)
8913.1	$\frac{63}{2}^+ \rightarrow \frac{59}{2}^+$	872.9	60(14)	
9839.6	$\frac{67}{2}^+ \rightarrow \frac{63}{2}^+$	926.5	45(12)	
10819.8	$\frac{71}{2}^+ \rightarrow \frac{67}{2}^+$	980.2	20(8)	
11854.5	$\frac{75}{2}^+ \rightarrow \frac{71}{2}^+$	1034.7	12(5)	

Table A2—continued

Level energy (keV)	$I_i^\pi \rightarrow I_f^\pi$	Transition energy (keV)	Intensity	Branching ratio
12943.4	$\frac{79}{2}^+ \rightarrow \frac{75}{2}^+$	1088.9		
14086.4	$\frac{83}{2}^+ \rightarrow \frac{79}{2}^+$	1143.0		
15284.3	$\frac{87}{2}^+ \rightarrow \frac{83}{2}^+$	1197.8		
16532.8	$\frac{91}{2}^+ \rightarrow \frac{87}{2}^+$	1248.5		
Band TSD3				
3863.6	$\frac{33}{2}^+ \rightarrow \frac{29}{2}^+$	(962.8)	< 15	
4369.1	$\frac{37}{2}^+ \rightarrow \frac{33}{2}^+$	505.5	26(10)	
	$\frac{37}{2}^+ \rightarrow \frac{33}{2}^+$	(1018.1)	< 15	
4937.1	$\frac{41}{2}^+ \rightarrow \frac{37}{2}^+$	568.0	32(6)	
	$\frac{41}{2}^+ \rightarrow \frac{37}{2}^+$	1070.8	10(3)	0.31(11)
5564.2	$\frac{45}{2}^+ \rightarrow \frac{41}{2}^+$	626.8	51(10)	
	$\frac{45}{2}^+ \rightarrow \frac{41}{2}^+$	1119.2	13(3)	0.25(8)
	$\frac{45}{2}^+ \rightarrow \frac{43}{2}^+$	(476.0)	< 8	< 0.16
6249.3	$\frac{49}{2}^+ \rightarrow \frac{45}{2}^+$	685.1	62(12)	
	$\frac{49}{2}^+ \rightarrow \frac{45}{2}^+$	1165.3	< 15	
6990.4	$\frac{53}{2}^+ \rightarrow \frac{49}{2}^+$	741.2	47(9)	
7786.3	$\frac{57}{2}^+ \rightarrow \frac{53}{2}^+$	795.9	41(8)	
8636.1	$\frac{61}{2}^+ \rightarrow \frac{57}{2}^+$	849.8	36(8)	
9538.6	$\frac{65}{2}^+ \rightarrow \frac{61}{2}^+$	902.5	25(6)	
10494.4	$\frac{69}{2}^+ \rightarrow \frac{65}{2}^+$	955.8	17(5)	
11503.6	$\frac{73}{2}^+ \rightarrow \frac{69}{2}^+$	1009.2	12(4)	
12566.6	$\frac{77}{2}^+ \rightarrow \frac{73}{2}^+$	1063.0	< 10	
13679.0	$\frac{81}{2}^+ \rightarrow \frac{77}{2}^+$	1112.4	< 10	

Table A2—continued

Level energy (keV)	$I_i^\pi \rightarrow I_f^\pi$	Transition energy (keV)	Intensity
Band TSD4			
6319.9	$\rightarrow \frac{45}{2}^+$	(1235.9)	< 15
6964.9		(645.0)	< 25
	$\rightarrow \frac{49}{2}^+$	(1184.0)	< 15
7667.1		702.2	25(16)
	$\rightarrow \frac{53}{2}^+$	(1133.6)	< 15
8421.7		754.6	30(15)
	$\rightarrow \frac{57}{2}^+$	(1082.6)	< 15
9231.7		810.1	25(10)
10097.0		865.3	20(10)
11017.6		920.5	15(9)
11993.3		975.7	< 15
13024.9		1031.6	–
14110.4		(1085.5)	–

References

- [1] W. Schmitz, C.X. Yang, H. Hübel, A.P. Byrne, R. Müsseler, N. Singh, K.H. Maier, A. Kuhnert, R. Wyss, Nucl. Phys. A 539 (1992) 112.
- [2] W. Schmitz, H. Hübel, C.X. Yang, G. Baldsiefen, U. Birkental, G. Fröhlingsdorf, D. Mehta, R. Müsseler, M. Neffgen, P. Willsau, J. Gascon, G.B. Hagemann, A. Maj, D. Müller, J. Nyberg, M. Piiparinen, A. Virtanen, R. Wyss, Phys. Lett. B 303 (1993) 230.
- [3] H. Schnack-Petersen, R. Bengtsson, R.A. Bark, P. Bosetti, A. Brockstedt, H. Carlsson, L.P. Ekström, G.B. Hagemann, B. Herskind, F. Ingebreetsen, H.J. Jensen, S. Leoni, A. Nordlund, H. Ryde, P.O. Tjøm, C.X. Yang, Nucl. Phys. A 594 (1995) 175.
- [4] C.X. Yang, X.G. Wu, H. Zheng, X.A. Liu, Y.S. Chen, C.W. Shen, Y.J. Ma, J.B. Lu, S. Wen, G.S. Li, S.G. Li, G.J. Yuan, P.K. Weng, Y.Z. Liu, Eur. Phys. J. A 1 (1998) 237.
- [5] S. Törmänen, S.W. Ødegård, G.B. Hagemann, A. Harsmann, M. Bergström, R.A. Bark, B. Herskind, G. Sletten, P.O. Tjøm, A. Görgen, H. Hübel, B. Aengenvoort, U.J. van Severen, C. Fahlander, D. Napoli, S. Lenzi, C. Petrache, C. Ur, H.J. Jensen, H. Ryde, R. Bengtsson, A. Bracco, S. Frattini, R. Chapman, D.M. Cullen, S.L. King, Phys. Lett. B 454 (1999) 8.
- [6] H. Amro, P.G. Varmette, W.C. Ma, B. Herskind, G.B. Hagemann, G. Sletten, R.V.F. Janssens, M. Bergström, A. Bracco, M. Carpenter, J. Domscheit, S. Frattini, D.J. Hartley, H. Hübel,

- T.L. Khoo, F. Kondev, T. Lauritsen, C.J. Lister, B. Million, S.W. Ødegård, R.B. Piercey, L.L. Riedinger, K.A. Schmidt, S. Siem, I. Wiedenhöver, J.A. Winger, *Phys. Lett. B* 506 (2001) 39.
- [7] G. Schönwasser, H. Hübel, G.B. Hagemann, J. Domscheit, A. Görgen, B. Herskind, G. Sletten, J.N. Wilson, D.R. Napoli, C. Rossi-Alvarez, D. Bazzacco, R. Bengtsson, H. Ryde, P.O. Tjøm, S.W. Ødegård, *Eur. Phys. J. A*, in press.
- [8] T. Bengtsson, *Nucl. Phys. A* 496 (1989) 56;
T. Bengtsson, *Nucl. Phys. A* 512 (1990) 124.
- [9] R. Bengtsson, www.matfys.lth.se/~ragnar/ultimate.html.
- [10] A. Bohr, B.R. Mottelson, *Nuclear Structure*, Vol. II, Benjamin, Reading, MA, 1975.
- [11] S.W. Ødegård, G.B. Hagemann, D.R. Jensen, M. Bergström, B. Herskind, G. Sletten, S. Törmänen, J.N. Wilson, P.O. Tjøm, I. Hamamoto, K. Spohr, H. Hübel, A. Görgen, G. Schönwasser, A. Bracco, S. Leoni, A. Maj, C.M. Petrache, P. Bednarczyk, D. Curien, *Phys. Rev. Lett.* 86 (2001) 5866.
- [12] J. Simpson, *Z. Phys. A* 358 (1997) 139.
- [13] J. Domscheit, S. Törmänen, B. Aengenvoort, H. Hübel, R.A. Bark, M. Bergström, A. Bracco, R. Chapman, D.M. Cullen, C. Fahlander, S. Frattini, A. Görgen, G.B. Hagemann, A. Harsmann, B. Herskind, H.J. Jensen, S.L. King, S. Lenzi, D. Napoli, S.W. Ødegård, C. Petrache, H. Ryde, U.J. van Severen, G. Sletten, P.O. Tjøm, C. Ur, *Nucl. Phys. A* 660 (1999) 381.
- [14] D.C. Radford, *NIM A* 361 (1995) 297.
- [15] J.N. Wilson, B. Herskind, *NIM A* 455 (2000) 612.
- [16] T. Yamazaki, *Nucl. Data, Sect. A* 3 (1967) 1.
- [17] R.D. Firestone, *Table of Isotopes*, Vol. II, Wiley, New York, 1996.
- [18] I. Hamamoto, *Nucl. Phys. A* 271 (1976) 15.
- [19] I. Hamamoto, B. Mottelson, *Phys. Lett. B* 127 (1983) 281.
- [20] I. Hamamoto, *Phys. Lett. B* 193 (1987) 399.
- [21] I. Hamamoto, B. Mottelson, *Phys. Lett. B* 132 (1983) 7.